PHYSICAL REVIEW D

PARTICLES AND FIELDS

THIRD SERIES, VOLUME 49, NUMBER 11 1 JUNE 1994

ARTICLES

Measurement of kinematic and nuclear dependence of $R = \sigma_L/\sigma_T$ in deep inelastic electron scattering

S. Dasu,* P. de Barbaro, A. Bodek, H. Harada,† M. W. Krasny,‡ K. Lang,§ and E. M. Riordan‖
University of Rochester, Rochester, New York 14627

L. Andivahis, R. Arnold, D. Benton,¶ P. Bosted, G. deChambrier, A. Lung,** S. E. Rock, and Z. M. Szalata
The American University, Washington, D.C. 20016

R. C. Walker,†† B. W. Filippone, J. Jourdan,‡‡ R. Milner,§§ R. McKeown, and D. Potterveld‖‖
California Institute of Technology, Pasadena, California 91125

A. Para
Fermi National Accelerator Laboratory, Batavia, Illinois 60510

F. Dietrich and K. Van Bibber
Lawrence Livermore National Laboratory, Livermore, California 94550

J. Button-Shafer, B. Debebe, and R. S. Hicks
University of Massachusetts, Amherst, Massachusetts 01003

R. Gearhart and L. W. Whitlow¶¶
Stanford Linear Accelerator Center, Stanford, California 94305

J. Alster
University of Tel-Aviv, Ramat Aviv, Tel-Aviv 69978, Israel

(Received 4 November 1993)

We report results on a precision measurement of the ratio $R = \sigma_L/\sigma_T$ in deep inelastic electron-nucleon scattering in the kinematic range $0.2 \leq x \leq 0.5$ and $1 \leq Q^2 \leq 10$ (GeV/c)^2. Our results show, for the first time, a clear falloff of R with increasing Q^2. Our R results are in agreement with QCD predictions only when corrections for target mass effects and some additional higher twist effects are included. At small x, the data on R favor structure functions with a large gluon contribution. We also report results on the differences $R_A - R_D$ and the cross section ratio σ^A/σ^D between Fe and Au nuclei and the deuteron. Our results for $R_A - R_D$ are consistent with zero for all x, Q^2 indicating that possible contributions to R from nuclear higher twist effects and spin-0 constituents in nuclei are not different from those in nucleons. The ratios σ^A/σ^D from all recent experiments, at all x, Q^2 values, are now in agreement.

PACS number(s): 13.60.Hb, 12.38.Qk, 25.30.Fj

---

[*] Present address: Department of Physics, University of Wisconsin, Madison, WI 53706.

[†] Present address: Mitsubishi Electric Co., Kokusai Bldg, Rm 730, 3-1-1 Marunouchi, Chiyoda-ku, Tokyo 100, Japan.

[‡] Present address: IN 2P3 - CNRS, Universites Paris VI et VII, Paris, France.

[§] Present address: Department of Physics, University of Texas, Austin, TX 78712.

[‖] Present address: Stanford Linear Accelerator Center, Stanford, CA 94309.

[¶] Present address: Department of Physics, University of Pennsylvania, Philadelphia, PA 19104.

[**] Present address: California Institute of Technology, Pasadena, CA 91125.

[††] Present address: Department of Physics, University of Rochester, Rochester, NY 14627.

[‡‡] Present address: Department of Physics, CH-4056, Basel, Switzerland.

[§§] Present address: Department of Physics, MIT, Cambridge, MA 02138.

[‖‖] Present address: Argonne National Laboratory, Argonne, IL 60439-4843.

[¶¶] Present address: MEC Laboratory, Daikin Industries, Tsukuba, Japan 305.

0556-2821/94/49(11)/5641(30)/$06.00

I. INTRODUCTION

The process of lepton-nucleon scattering has proven to be an effective tool in probing the structure of nucleons. In this process the leptonic part of the interaction can be accurately calculated within the framework of quantum electrodynamics, and hence the results can be interpreted solely in terms of the structure of the probed nucleons. There are two structure functions F_1 and F_2 which parametrize the hadronic vertex in this scattering. Naive parton model predictions of the scale independence of F_1 and F_2 at large values of momentum transfer, and a simple kinematic relation between F_1 and F_2, were consistent with early experiments [1–3]. In more accurate later experiments, scaling violations have been observed at moderate values of momentum transfer [4,5]. These experiments have, however, left open the precise form of the relationship between F_1 and F_2.

The ratio $R = \sigma_L/\sigma_T$ of the longitudinal (σ_L) and transverse (σ_T) virtual photon absorption cross sections is the quantity that expresses the relation between the two structure functions in a convenient form. R yields information about the spin and the transverse momentum of the nucleon constituents. In a model with spin-1/2 partons, R is expected to be small, and to decrease rapidly with increasing momentum transfer, Q^2. With spin-0 partons, R should be large and increase with Q^2. Previous measurements [3–5] of R at the Stanford Linear Accelerator Center (SLAC) indicated that scattering from spin-1/2 constituents (e.g., quarks) dominates. However, in the SLAC kinematic range, the values of R were larger than expected, and were consistent with a constant value of 0.2. The measurement errors on those results left room for speculation about small admixtures of spin-0 constituents in nucleons [6,7] (e.g., tightly bound diquarks), and about the unexpectedly large primordial transverse momentum for quarks. Within the framework of quantum chromodynamics (QCD), logarithmic scaling violations [8] occur due to quark-gluon interactions. In particular, within QCD, the value of R is proportional to the QCD coupling strength α_s, which decreases with increasing Q^2, while the shape at low x is sensitive to the gluon distribution. Therefore, good measurements of R, at high Q^2, can provide important constraints on the gluon distribution. In addition, at lower Q^2 target-mass [9–13] and dynamical higher twist effects [14], i.e., nonperturbative effects due to binding of quarks in a nucleon, yield power-law violations of scaling. These effects lead to nonzero contributions to R which decrease with increasing Q^2. Accurate knowledge of R is essential to test these predictions, and to derive F_2 from cross sections, at moderate values of momentum transfer.

The discovery of the difference in the deep inelastic cross sections for iron and deuterium targets [15–18], known as the European Muon Collaboration (EMC) effect, has sparked considerable activity in the theoretical study of deep inelastic lepton scattering from nuclear targets. There are numerous models [19] for the EMC effect, built on a variety of ideas. All these models explain the change of quark distributions in nuclei compared to those in free nucleons. Some of these models involve a swelling of nucleons bound in a nucleus, or Q^2 rescaling, and others involve the presence of tightly bound pions or Δ isobars, or multiquark clusters in nuclei. The least drastic of these models attribute the EMC effect to nuclear binding corrections alone. To compare the theoretical predictions for the structure function ratio with the experimental results on the cross section ratio, it is important to measure the differences in R for various nuclear targets. Some models [20] predict a large difference in the quantity R for deuterium and iron ($R_{\mathrm{Fe}} - R_D \approx 0.1 - 0.15$). Others [21,22], including those based on QCD, predict a negligible difference ($R_{\mathrm{Fe}} - R_D \approx 0.002$). Some authors [23] have conjectured that higher twist effects might be different for different nuclei, and yield an atomic mass (A) dependence of R. Since R is a sensitive measure of pointlike spin-0 constituents (e.g., tightly bound diquarks) of the nucleus, an A dependence of R could alter our view of nuclear structure in terms of spin-1/2 quarks and vector gluons.

Since the quality of the previous data was inadequate to test such predictions for R, we have made precision measurements of deep inelastic electron-nucleon scattering cross sections from D, Fe, and Au targets, with particular emphasis on the extraction of the ratio R, and precise absolute normalization of cross sections. The SLAC electron beams and the 8 GeV spectrometer facility were used to measure cross sections accurate to ±1% in a large kinematic range. Extensive efforts were made in this experiment to reduce systematic effects, especially those that contribute to the measurement of R. Radiative corrections to the data were studied carefully using various techniques and considerable improvements were made. The results from this experiment, previously published as letters, have shown that there is a clear kinematic dependence of R [24], and that $R_A - R_D$ is consistent with zero [25]. The results obtained from these data, and improvements made to the radiative correction calculation programs, and improvements in the overall normalization, have been essential in the reanalysis of entire SLAC deep inelastic data sets [26–28].

The differential cross section for scattering of an unpolarized charged lepton with an incident energy E_0, final energy E', and scattering angle θ can be written in terms of the structure functions F_1 and F_2 as

TABLE I. Kinematic range of this experiment.

x	Q^2	No. of ϵ points	ϵ_{min}	ϵ_{max}	Targets
0.20	1.0	5	0.49	0.85	D,Fe(6%),Fe(2.6%),Au
	1.5	5	0.48	0.80	D,Fe(6%)
	2.5	3	0.35	0.72	D,Fe(6%)
	5.0	4	0.32	0.57	D
0.35	1.5	5	0.60	0.84	D,Fe(6%)
	2.5	5	0.51	0.87	D,Fe(6%)
	5.0	4	0.45	0.78	D,Fe(6%)
0.50	2.5	5	0.42	0.93	D,Fe(6%),Fe(2.6%)
	5.0	4	0.40	0.93	D,Fe(6%)
	7.5	2	0.37	0.74	D
	10.0	3	0.35	0.70	D

$$\frac{d^2\sigma}{d\Omega dE'}(E_0,E',\theta)=\frac{4\alpha^2E'^2}{Q^4}\cos^2(\theta/2)\left[F_2(x,Q^2)/\nu+2\tan^2(\theta/2)F_1(x,Q^2)/M\right], \tag{1}$$

where α is the fine structure constant, M is the nucleon mass, $\nu = E_0 - E'$ is energy of the virtual photon which mediates the interaction, $Q^2 = 4E_0E'\sin^2(\theta/2)$ is the invariant four-momentum transfer squared, and $x = Q^2/2M\nu$ is a measure of the longitudinal momentum carried by the struck partons. For simplicity, the differential cross section is often denoted just by σ.

Alternatively, one could view this process as virtual photon absorption. Unlike the real photon, the virtual photon can have two modes of polarization. In terms of the cross section for the absorption of transverse (σ_T) and longitudinal (σ_L) virtual photons, the differential cross section can be written as

$$\frac{d^2\sigma}{d\Omega dE'}=\Gamma\left[\sigma_T(x,Q^2)+\epsilon\sigma_L(x,Q^2)\right], \tag{2}$$

where

$$\Gamma=\frac{\alpha KE'}{4\pi^2Q^2E_0}\left(\frac{2}{1-\epsilon}\right), \tag{3}$$

$$\epsilon=\left[1+2\left(1+\frac{Q^2}{4M^2x^2}\right)\tan^2\frac{\theta}{2}\right]^{-1}, \tag{4}$$

$$K=\frac{2M\nu-Q^2}{2M}. \tag{5}$$

The quantities Γ and ϵ represent the flux and the degree of longitudinal polarization of the virtual photons, respectively. The quantity R is defined as the ratio σ_L/σ_T, and is related to the structure functions by

$$R(x,Q^2)=\frac{\sigma_L}{\sigma_T}=\frac{F_2}{2xF_1}\left(1+\frac{4M^2x^2}{Q^2}\right)-1=\frac{F_L}{2xF_1}, \tag{6}$$

where F_L is called the longitudinal structure function. The structure functions are expressed in terms of σ_L and σ_T as

$$F_1=\frac{MK}{4\pi^2\alpha}\sigma_T, \tag{7}$$

$$F_2=\frac{\nu K(\sigma_L+\sigma_T)}{4\pi^2\alpha(1+\frac{Q^2}{4M^2x^2})}, \tag{8}$$

and

$$F_L(x,Q^2)=F_2\left(1+\frac{4M^2x^2}{Q^2}\right)-2xF_1. \tag{9}$$

The kinematic range of this experiment is shown in Table I.

II. EXPERIMENTAL APPARATUS

A. Upstream beam system

Electrons from both the Main Injector and the Nuclear Physics Injector [29] (NPI) at SLAC [30] were used

TABLE II. Typical systematic errors on the results.

Source	Uncertainty	Error(±)			
	(±)	$\Delta\sigma$	ΔR	$\Delta(\sigma_A/\sigma_D)$	$\Delta(R_A-R_D)$
Incident energy	0.1%	0.3%	0.014	0.3%	0.014
Beam steering	0.003°	0.1%	0.005	0.1%	0.004
Charge measurement	0.2%	0.2%	0.009	0.1%	0.004
D target density	0.3%	0.3%	0.014	0.3%	0.014
Scattered energy	0.05%	0.1%	0.005	-	-
Spectrometer angle	0.002°	0.1%	0.005	-	-
Acceptance vs p	0.1%	0.1%	0.005	-	-
D acceptance vs θ	0.1%	0.1%	0.005	0.1%	0.004
Detector efficiency	0.1%	0.1%	0.005	-	-
e^+/e^- background	0.1%	0.1%	0.005	0.1%	0.004
Total point to point		0.5%	0.025	0.5%	0.021
Incident energy	0.1%	0.3%	0.014	-	-
Charge measurement	0.5%	0.5%	-	-	-
Target length	0.8%	0.8%	-	0.9%	-
Scattered energy	0.04%	0.1%	0.005	-	-
Spectrometer angle	0.006°	0.2%	0.009	-	-
Acceptance	1.0%	1.0%	-	-	-
Rad. corr. ϵ dep.	1.0%	1.0%	0.025	-	0.015
Rad. corr. norm.	1.0%	1.0%	-	0.5%	-
Fe/Au neutron excess	0.2%	-	-	0.2%	-
Total normalization		2.0%	0.030	1.1%	0.015

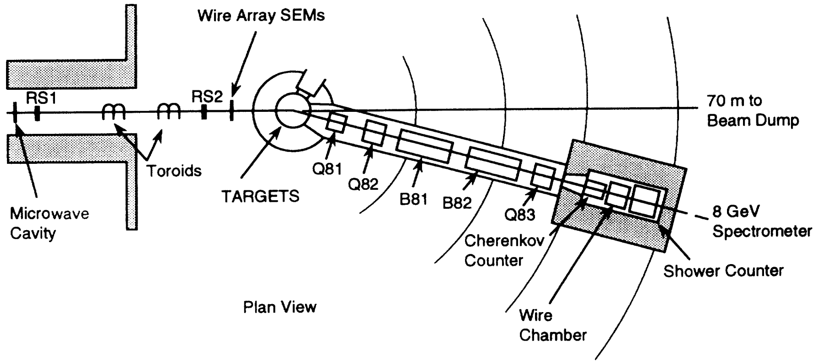

FIG. 1. Floor plan of the experimental hall showing the beam line components, target, and the 8 GeV spectrometer with detectors.

in this experiment. The Main Injector is located at the beginning of the beam line approximately 2 miles from the experimental hall. Utilizing all 30 "sectors" of the linac with this injector, electron energies between 5 and 21 GeV can be achieved with peak currents ≤ 40 mA. At the lower energies (< 6 GeV), the peak current is reduced due to the effects of beam breakup along the accelerator line. The NPI was installed to provide high current beams at these lower energies and is located six sectors from the linac exit. It can provide beams of ≈ 40 mA peak current with energies between 0.65 and 4.5 GeV, and was therefore used at beam energies ≤ 4.25 GeV. The Main Injector was used at the higher energies. Beam pulses were typically 1.6 μs in width and were operated between 60 and 90 Hz.

The beam was directed into the "A line" for delivery to End Station A (ESA). The energy of the beam was defined in the "A bend," a set of eight identical dipole magnets that bent the beam in a horizontal plane through a set of slits. These slits defined the energy spread of the beam, which was adjusted to be between 0.1 and 0.5% full width, in this experiment. For monitoring purposes, an additional identical dipole magnet, in series with the others, was maintained separate from the beam line. A rotating flip coil, which was located at the nominal beam position inside this magnet, continuously monitored the field strength. The original calibration of the A-bend optics quoted an absolute calibration uncertainty of $\pm 0.1\%$. This was confirmed by a recent recalibration [31]. Analysis of elastic peak positions indicated typical fluctuations of the central value of the beam energy of $\pm 0.05\%$ with typical uncertainty of $\pm 0.03\%$. Table II shows these and other systematic errors.

Final steering of the beam to the target was accomplished by sending the beam through two sets of vertical and horizontal bending magnets after it left the A bend. The first set of magnets was located ≈ 100 m upstream of the target; the second set was located ≈ 50 m upstream. A set of two resonant microwave cavities were located immediately following the second set of magnets to measure the horizontal and vertical beam position. Two secondary emission wire arrays were located in the beam path ~ 1 m upstream of the target (see Fig. 1). An LSI-11 microcomputer continuously monitored the beam position at the cavity monitors and wire arrays throughout the experiment. This computer also controlled the current in a set of smaller auxiliary coils around the steering magnets, and maintained the beam along the nominal

TABLE III. Length measurements for solid and liquid targets are given in units of radiation length or centimeters. Thickness of material before and after target is also given.

Liquid target dimensions			
Component	Deuterium	Hydrogen	Empty replica
Target length (cm)	20.086	19.972	20.045
Al flow separator (r.l.)	0.000288	0.000288	0.000288
Al cell wall (r.l.)	0.000864	0.000864	0.000864
Mylar insulation (r.l.)	0.000221	0.000221	0.000221
Al front end cap (r.l.)	0.000864	0.000864	0.014001
Al back end cap (r.l.)	0.000864	0.000864	0.014001
Solid target dimensions			
Target	Thickness		
Fe 6.0% (cm)	0.1067		
Fe 2.6% (cm)	0.0470		
Au 6.0% (cm)	0.0198		
Material before/after target			
Component	Thickness		
Before target (r.l.)	0.00103		
After target (r.l.)	0.00940		

beam axis continuously throughout the data taking. The typical uncertainty was ±0.003° in the incident beam angle, and ±0.1 cm in the beam position at the target.

Two zinc-sulfide (ZnS) roller screens, separated by ~ 10 m, were located upstream of the target in ESA and could be rolled into the beam line at low beam pulse rates between data runs. The beam position could be observed on these roller screens by the experimenters through remote TV cameras. A ZnS target could also be inserted at the target position to allow the beam position to be observed. Thus, the experimenters could confirm that the beam transport system was operating properly.

The total amount of incident charge in the beam was measured with a set of two identical ferromagnetic toroidal charge monitors placed around the beam line upstream of the target [32]. Two independent systems located in the counting house amplified and analyzed the signals from resonant circuits driven by the toroids. One of these systems measured the integral of one-half cycle of the signal, and the other sampled the peak of the pulse. These results were accumulated and periodically stored on magnetic tape.

The toroids were calibrated by sending a pulse of charge through a wire that passed through the toroids. A capacitor was charged to a nominal voltage with a digital-to-analogue converter and was discharged through the wire. An additional attenuator circuit was located near the toroids and was remotely set to allow for either large or small beam currents to be simulated. The resulting signal of the toroids was measured and the relationship between the incident charge and signal pulse could be determined. Separate calibration systems were used for each toroid. This system was used to monitor any changes in the toroid system caused by temperature fluctuations, drifts in the amplifier gains, and shifts in the timing. Calibration measurements were done every few hours, between data runs. Comparisons between the two toroids indicated run to run fluctuations of ±0.2%. Previous comparisons with a Faraday cup [33], as well as agreement of the two toroid systems indicate an absolute uncertainty of ±0.5%.

B. Targets

Liquid hydrogen and deuterium targets, an empty liquid target replica, two iron targets and a gold target, were used in this experiment [34]. Table III summarizes the dimensions of these targets and materials that were used in housing them.

The cylindrical liquid targets were 20 cm in length and 5.08 cm in diameter. Their side walls, entrance, and exit windows were made of 0.076 mm aluminum. The empty target replica was identical to the full cell, except for an additional 1.16 mm of aluminum radiator added to both the entrance and exit windows. This empty target replica was used to measure end cap contributions to the scattering. The additional aluminum was added to make the radiation lengths of the empty cells roughly equal to that of the full deuterium cell, to increase the scattering rate, and to reduce the time needed to measure end cap contribution [35].

Liquid hydrogen and deuterium at a temperature of 21 K, and a pressure of 2 atm was pumped continuously through the targets. Heat deposited by the beam was removed by circulating the liquids through heat exchangers. Contamination levels within the hydrogen were measured by mass spectroscopy to be $\approx 0.16\%$ deuterium; and in the deuterium to be $\approx 2\%$ hydrogen. A 4 cm diameter aluminum tube 0.025 mm thick was contained within the cells and was used as a flow guide. The liquid went into the target inside this flow guide and exited between the flow guide and the outer target wall. Circulation was maintained by fanlike pumps at a flow rate ~ 1 m/s. During part of the experiment, the flow direction through the 20 cm hydrogen cell was accidentally reversed. Unfortunately, the hydrogen target was rendered useless in obtaining inelastic data because of an

TABLE IV. 8 GeV spectrometer transport coefficients used to reconstruct electron kinematics at the target. Target quantities are denoted by subscript "t" and spectrometer quantities are denoted by subscript "s" in this table. For example, $x_t = 4.553\,62x_s - 4.291\,85\theta_s \ldots - 0.000\,05\phi_s^2 + 0.162\,11$.

	x_t	θ_t	ϕ_t	δ_t
x_s	4.55362	0.19387	-0.03694	-0.00205
θ_s	-4.29185	0.02408	0.03954	0.00245
y_s	-0.06007	0.00050	-0.02689	-0.34275
ϕ_s	-0.00142	-0.00419	-0.92820	0.00074
x_s^2	0.01756	0.00051	0.01063	-0.00013
$x_s\theta_s$	-0.03237	-0.00103	-0.01993	0.00012
$x_s y_s$	-0.00492	0.01485	0.00034	0.00059
$x_s\phi_s$	0.00133	-0.00098	0.00056	0.00005
θ_s^2	0.01543	0.00051	0.00930	0.00000
$\theta_s y_s$	0.00850	-0.01421	-0.00037	-0.00059
$\theta_s\phi_s$	-0.00106	0.00082	-0.00052	-0.00003
y_s^2	-0.00411	-0.00012	-0.00525	0.00020
$y_s\phi_s$	-0.00019	0.00003	-0.00083	0.00136
ϕ_s^2	-0.00005	0.00001	-0.00009	0.00004
Offset	0.16211	0.00169	0.00171	0.00044

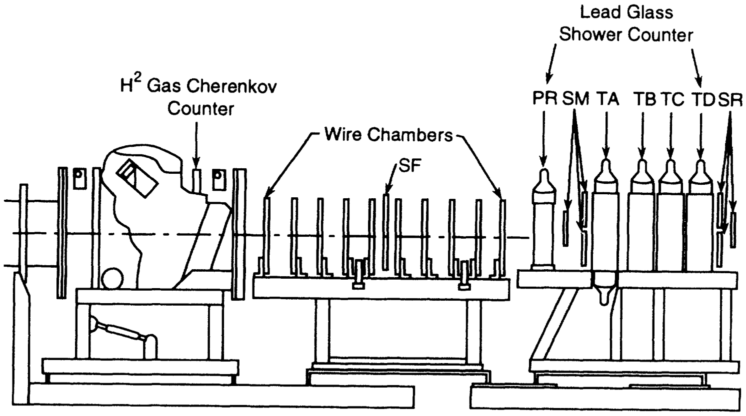

FIG. 2. Cross sectional representation of our detector package showing Cherenkov counter, wire chambers, scintillation counters, and lead-glass shower counter.

unknown amount of flow guide aluminum in the electron path. It was possible to correct for this problem in the elastic scattering data from the hydrogen cell. The effects of this reversed flow on the elastic hydrogen data are discussed in detail elsewhere [32,36].

Vapor pressure bulbs and platinum resistors were located at the entrance and exit of the flow guides to measure the temperature. The ingoing and outgoing density was calculated from these measurements, and the pressure of the liquid, and was monitored every 10 s. Average density changes in the deuterium target due to beam heating were never more than 0.7%, and corrections to the cross sections were applied to take them into account. Local density fluctuations, due to possible boiling along the beam axis, were measured by comparing cross sections taken at both large and small beam currents for the same kinematic setting. The variation in cross sections was less than the statistical errors in these data, and it resulted in an uncertainty of ±0.3% at nominal beam current and duty cycle [37].

The solid targets consisted of two iron targets, of 2.6% and 6% radiation lengths, and, a gold target of 6% radiation length. Target thicknesses (see Table III) were measured using precision gauges before and after the experiment to an accuracy of ±0.0005 cm. Thermocouples were connected to the targets to measure the temperature during the data taking. Comparisons were made between the cross sections measured with the two iron targets to check the accuracy of the external radiative corrections. Most of the solid target data was taken with the 6% radiation length iron target.

These targets were mounted on a remotely controlled carousel that could be moved vertically and rotated in a horizontal plane to place any desired target into the beam line. This assembly was contained under vacuum within a scattering chamber that was an aluminum cylinder with 2.54 cm thick walls. The beam entered the scattering chamber through a 12.7 cm circular aperture made of 0.025 mm aluminum that isolated the chamber vacuum from the beam line vacuum. An extended snout attached to the scattering chamber allowed for electrons scattering at angles $11^\circ < \theta < 50^\circ$ to exit the chamber through a thin 0.31 mm exit window.

C. Spectrometer

After the electrons scattered from the target, they were detected in the 8 GeV spectrometer [38] in the ESA (see Fig. 1). Electrons were focused and momentum selected by a series of three quadrupole and two vertical-bend dipole magnets. Immediately after the last magnet was a lead-shielded concrete hut in which the particle detectors were located. The spectrometer could be rotated around the target pivot on a horizontal circular track to allow only those electrons which had scattered at the desired angle to reach the detectors.

The energy of the electrons entering the spectrometer is given by $E' = p(1 + \Delta p/p)$, where p is the central momentum setting. The magnets of the spectrometer were tuned to focus particles with energy E' and angle θ to vertical and horizontal positions, respectively, in the detector hut. Central values of $1 \le p \le 8$ GeV and $11.5^\circ \le \theta \le 48^\circ$ were used in this experiment. The difference between the central spectrometer angle and the projected horizontal angle is given by $\Delta\theta$. The vertical angle with respect to the spectrometer plane is given

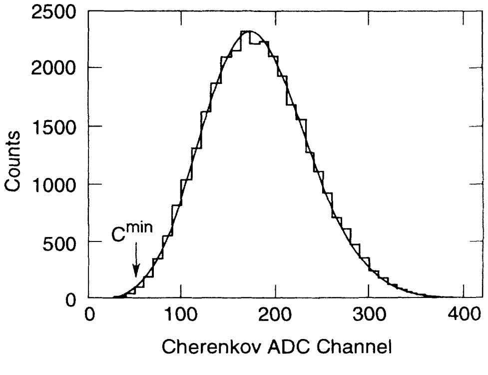

FIG. 3. Cherenkov counter spectrum for an elastic scattering data run, i.e., for electron rich run, is shown. $C^{\min} = 50$ is the value of Cherenkov counter cut used to select electrons in the analysis.

by ϕ. Measured positions and angles of tracks in the detector were transformed to $\Delta p/p$, $\Delta\theta$, and ϕ, using spectrometer optics coefficients given in Table IV. The spectrometer had good acceptance in the region $\pm3.6\%$ in $\Delta p/p$, ±6 mr in $\Delta\theta$, and ±28 mr in ϕ. Calibration and acceptance of the spectrometer are discussed in detail in Appendix A.

D. Detectors

The detector package was designed to detect electrons with $> 99\%$ efficiency and reject pions to one part in 10^5, in order to avoid large systematic uncertainties due to efficiency corrections or pion backgrounds (π/e ratios were sometimes as high as 100:1). It was also required to measure both the position and angle of the particle tracks to ±2 mm and ±1 mr, respectively. These goals were achieved with three essential elements: a hydrogen gas threshold Cherenkov counter, a set of ten multiwire proportional chambers, and a Pb-glass total absorption array (see Fig. 2). Three sets of plastic scintillators were also included to add to the spatial segmentation of the detectors, to serve as fast trigger elements, and to assist in pion identification and rejection.

The Cherenkov counter entrance window was located at the end of the last quadrupole magnet of the spectrometer. The entrance and exit windows were made from thin aluminum sheets. The counter was 3.3 m long and was filled with hydrogen at atmospheric pressure. A set of four curved mirrors with total area of 53 by 90 cm was located 315 cm from the entrance window, and was used to focus the Cherenkov radiation onto the face of a RCA 8854 phototube located at the top of the counter. The mirror was made of 0.64 cm backing of Lucite with aluminum coating, resurfaced with a layer of MgF_2 to eliminate oxidation on the surface. It was aligned within the counter with a laser to ensure that the Cherenkov light was properly focused onto the phototube face. A wavelength shifter coating was applied to the face of the phototube to increase its sensitivity to the ultraviolet light.

Emphasis was placed on eliminating oxygen in the counter to allow for the detection of Cherenkov radiation emitted by electrons appearing in the ultraviolet part of the spectrum. The Cherenkov counter was purged weekly by evacuating to < 5 torr, filling with nitrogen, evacuating again, and refilling with hydrogen. Leaking of oxygen through the outer rim of the phototube face, and the rubber O ring against which it rested, was limited by overpressurizing the Cherenkov chamber hood to 1.5 atm with nitrogen.

A Cherenkov counter spectrum for an elastic scattering data run is shown in Fig. 3. Fitting the spectrum to a Poisson distribution indicated that 7.7 photoelectrons were typically produced, consistent with the expected number of 7–9 [32]. Electron detection efficiency is expected to be 99.75%, with a threshold below 1 photoelectron peak, based on these photostatistics. An analysis of events which deposited a large amount of energy in the shower counter, but did not require the Cherenkov counter in the trigger, indicated an efficiency of $\approx 99.7\%$. The π/e discrimination of the Cherenkov counter was measured to be $\sim 10^3$:1.

Following the Cherenkov counter were ten planes of multiwire proportional chambers, which are described in detail elsewhere [39]. The chambers had an active region 35 cm in height and 93 cm in width, and spanned 1.8 m in the direction of the particle trajectory. Chambers were numbered from one to ten sequentially along the direction of the scattered electrons. Even-numbered chambers had wires oriented along the horizontal direction to measure the vertical track position; they permitted a precise measurement of the particle momenta. Chambers 1, 5, and 9 had wires oriented at $-30°$ from the vertical; chambers 3 and 7 were oriented at $+30°$ (viewed along the particle trajectory). These chambers measured the horizontal track position, so that multiple tracks could be identified and separated. The spectrometer E' and θ focal planes were contained within the chamber area.

The detection efficiency of the individual wire chambers was measured to be $\sim$ 90–95 %. The efficiency of the tracking algorithm was derived from these individual efficiencies to be $\geq 99.9\%$. Analysis of events that clearly passed through the central area of the wire chambers (determined by taking advantage of spatial segmentation provided by other detector elements) also indicated a tracking efficiency in excess of 99.9%.

The Pb-glass total absorption counter was segmented both in the horizontal direction and along the particle trajectory. The first row of six F2-type Pb-glass blocks were used as a preradiator (PR) to start the electromagnetic shower. These blocks had a radiation length of 3.22 cm, and were 32 cm tall, 15.8 cm wide, and 10.4 cm thick. The maximum particle trajectory angle in the spectrometer was $\pm2.5°$ from the central axis, so the PR row was rotated by 5° around the vertical to eliminate the possibility of particles passing through the cracks between the blocks. XP 2041 phototubes were placed at the top of the blocks to detect Cherenkov radiation from the electromagnetic showers.

The next four rows of SF5-type Pb glass (TA, TB, TC, TD) were 40 cm high, 14.6 cm wide, and 14.6 cm thick. The first three rows had seven blocks, the last row had six. Each row was staggered relative to the next so that the cracks between the blocks did not overlap. Phototubes were placed on the top of each block. Since the shower maximum occurred near the first row of these blocks, an additional phototube was placed on the bottom of each of these blocks (called TAD) to maximize the shower detection efficiency and resolution. The total thickness of the shower counter was 30.4 radiation lengths. The rms resolution of the Pb-glass array was found to be $8\%/\sqrt{E'}$. The shower counter gave an additional π/e discrimination of 50:1, while still maintaining an efficiency for electron detection of $\geq 99.9\%$.

Plastic scintillators were used to detect all minimum ionizing particles. A row of six rectangular scintillators were placed vertically between wire chambers 7 and 8, to provide additional horizontal segmentation. Three scintillators were placed horizontally between the shower counter rows PR and TA, to provide additional vertical segmentation to the detectors. A final set of three horizontal scintillators were located behind the shower counter. These scintillators detected cosmic ray muons that were used for shower counter calibration runs. The three sets of scintillators were labeled SF, SM, and SR, respectively (see Fig. 2).

E. Electronics

Raw detector signals from the phototubes on the detectors were carried to the electronics in the counting house, ~ 100 m away by fast heliax cables (for trigger components) or regular coaxial cables (for other components). Commercially available CAMAC and NIM modules were used for the electronics. Attenuators were used to reduce the signals, from the shower counter rows PR, TAU, TAD, and TB, by 50% at $E' > 4$ GeV to keep the signals from saturating the electronics at large momenta, while maintaining reasonable resolution at small momenta.

A simplified schematic of the electronics is shown in Fig. 4. The electronic signals were divided using linear fan-out components. One output of the fan outs went to a set of analogue-to-digital converters (ADC's) to record pulse-height information. The other output was fed through discriminators to the trigger logic and other electronic elements. The outputs of the discriminators were set to a width of 20 ns. These pulses were sent to scalers, fast latches, and as stop gates to time-to-digital converters (TDC's). In addition, the raw signals of individual components of shower counter layers (PR1–6, TAD1–7, etc.) were linearly added together to form single pulses, which went to ADC's and discriminators and then to scalers, latches, and TDC's. Signals from individual SF scintillation counters, and time averaged left and right signals from SM scintillation counters (see Fig. 2), were sent to TDC's and scalers.

The trigger was designed to fulfill several different purposes. It was necessary that it be more than 99.9% efficient for electrons over the entire range of momenta measured, $1 \leq E' \leq 8$ GeV. Deep inelastic data were taken with π/e backgrounds of up to 100:1; thus the trigger needed to have a pion rejection of $> 99\%$ to keep the trigger rate from being dominated by background pion events. It was also of interest to have a limited measurement of the detector response to pions, so that the detector performance could be better understood.

The trigger for the experiment was set up to have very high efficiency for electrons, but it also included a prescaled sample of pions for background calculation, and some random triggers to permit ADC pedestal determination. High efficiency for electron trigger (EL-20; 20 ns pulse width) was achieved by using two separate triggers for low-energy and high-energy electrons. The high-energy electron trigger was composed of a three out of four coincidence amongst Cherenkov counter, preradiator PR, middle scintillation counter SM, and TAD row of shower counter (see Fig. 2). This combination had a very high efficiency for high-energy electrons, and was not affected by the pion background rate. However, for low-energy electrons, the electron shower was sometimes contained within the preradiator PR row of lead glass itself. To avoid corresponding reduction in efficiency, a low-energy electron trigger composed of 2/3 coincidence of PR, SF, and SM scintillation counter signals, in association with Cherenkov counter, was instituted to give increased efficiency for these energies. A coincidence of SF and SM scintillators provided the pion trigger (PION). This signal was then prescaled by a factor of 2^8 and included in the trigger. These events were only used for studying the detector response to pions. A random pulse generator signal (RANDOM) fired approximately every 10 s, and was included to monitor the pedestals of the ADC's. The coincidence of any of the three trigger components (EL-20, prescaled PION, RANDOM) with a beam gate generated a pretrigger. Since the data acquisition modules could record only one event for each 1.6 μs beam spill, the pretrigger signal went through a circuit which would allow the trigger to fire only once per beam pulse. The trigger provided the gates for the ADC's, generated start pulses for the TDC's, reset the latches, and interrupted the PDP computer to perform the event data logging. It also generated a gate signal for the wire chambers.

Additional pulses (EL-40, EL-60, and EL-80) were formed that were identical to EL-20 except for longer widths (40, 60, and 80 ns) in order to measure the effect of the electronic dead time on the trigger rate. The ideal trigger rate for a pulse width of 0 ns could be deduced from an extrapolation of the scaler rates of these pulses.

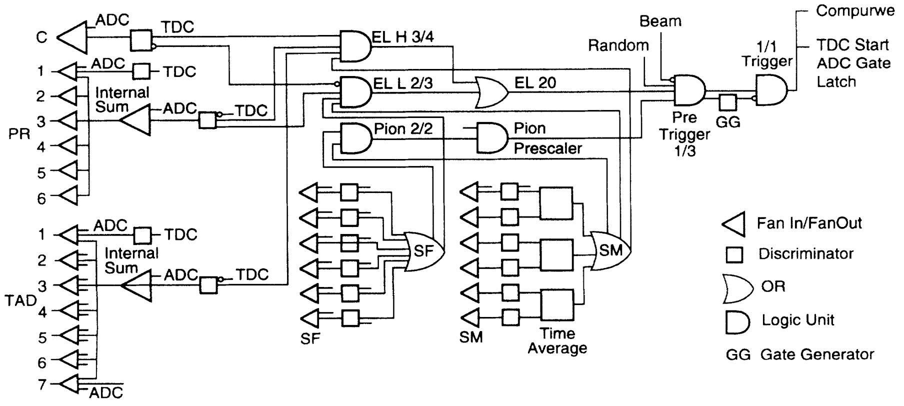

FIG. 4. Block diagram showing electronics and trigger setup for this experiment.

Electronics dead time was also measured using scalers of 3/3 coincidence of preradiator PR, TAD shower counter, and Cherenkov counter signals (PTC-20, PTC-40, PTC-60, PTC-80), which provided very high purity electron signal. Electronics dead time never exceeded 0.5%. The effect of limiting the trigger to firing once per 1.6 ms beam pulse was measured in various ways.

F. Data acquisition system

The data acquisition was performed by a PDP-11/04 computer which acted as a terminator to the UNIBUS of a Vax 11/780 computer. The PDP collected the data from CAMAC, and wrote it to the Vax memory buffer directly. The Vax in turn stored the data on magnetic tape. Information that needed to be monitored on a periodic basis, such as the spectrometer magnets, high voltage power supplies, accumulated scaler and toroid values, and the target positions, was acquired through CAMAC interfaces. The Vax could correct any drifts in the spectrometer magnets or high voltage power supplies.

Information from the beam steering system and the toroid accumulators was read by an LSI-11 minicomputer. In addition, the LSI steered the beam, cleared the toroid electronics, and controlled the toroid calibration system. The Vax 11-780 computer would periodically receive the accumulated information from the LSI-11 and record it on magnetic tape.

III. DATA ANALYSIS

A. Introduction

The data were reduced to results reported here in three major steps. In the first step electron scattering events were identified, and accumulated in $\Delta p/p$, $\Delta\theta$, and ϕ bins. Cross sections were calculated in the second step, including corrections for the spectrometer calibration and acceptance (see Appendix A), higher-order radiative processes (see Appendix B), dead time, and detector efficiencies. The final step was to perform a Rosenbluth separation of the cross sections at fixed (x, Q^2) but different ϵ values. The first step was identical for both the elastic and inelastic data sets. The analysis and results of the inelastic data are presented here while the elastic data are presented in the accompanying article [36].

B. Event analysis

The first goal of the event analysis was to determine the path the particle took through the detector package. This information was extracted primarily from the wire chamber data. The reverse transport coefficients of the spectrometer were then used to determine the momentum and trajectory of the event at the target pivot. Finally, cuts were placed on the pulse heights in the Cherenkov and total absorption counters to eliminate background pion events. Electron events were then stored in a three-dimensional histogram $N_e(\Delta p/p, \Delta\theta, \phi)$.

1. Track fitting

In order to find the particle trajectory through the wire chambers, all possible tracks between hit wires in different pairs of horizontally wired chambers were first calculated. Tracks that were clearly spurious, i.e., those that were far outside of the spectrometer acceptance, were ignored. The other chambers were checked for any wire hits within ±4 wires of each of the tracks. This yielded the vertical coordinates of all possible tracks. Using this information, a similar process was followed with the vertically wired chambers to find all possible tracks in the horizontal direction. Only those tracks that had associated hits in at least six chambers, including two horizontally wired chambers and two vertically wired chambers, were considered. If only one track was found, it was recorded as the particle track.

Sometimes multiple tracks were found in the wire chambers. These tracks were mostly due to pions which entered the spectrometer in association with the triggered electron during the 100 ns long gate of the wire chambers. Some small fraction of them were also due to δ rays. The pion tracks were purged, and the "best" electron track was determined using the energy measurement and segmentation provided by the lead-glass shower counter. In the $< 0.1\%$ of cases where it was not possible to eliminate all but one track, one of the remaining tracks was chosen at random.

Coordinates in the spectrometer hut were defined by z along the nominal particle trajectory, y the vertical direction perpendicular to the particle trajectory, and x perpendicular to the y-z plane in a left-handed coordinate system. The particle track was parametrized in terms of its horizontal and vertical position (x and y) at the p focus, and its projected slope in the x-z and y-z planes (dx/dz and dy/dz). Tracks were then transformed back to the scattering point at the target, in terms of the horizontal ($\Delta\theta$), vertical (ϕ) angles, and fractional momentum ($\Delta p/p$). Second-order reverse transport coefficients, obtained by averaging 6 and 8 GeV data from a dark current run were used in this analysis. Those coefficients are shown in Table IV. Dark current experiment consisted of measuring the well-calibrated electron beams from the accelerator directly in the spectrometer. This required very low multiplicity electron beam bunches which were obtained by turning off the thermionic gun that normally supplies the electron bunches for the acceleration.

2. Electron identification

Four requirements were placed on each event in order for it to pass as a clean electron event. The first was that the electron trigger (EL-20) have fired. The trigger efficiency for electrons was determined to be $> 99.99\%$. One good track in the wire chambers was also required; this condition was also satisfied with high efficiency ($> 99.9\%$). The third requirement was that a pulse be observed from the Cherenkov counter above ADC channel 50. This provided the principal π/e separation, while maintaining good electron efficiency ($\sim 99.7\%$). Finally, the existence of a large energy deposition in the shower counter was required to provide additional π/e discrimination. This cut also had a high efficiency of $\sim 99.7\%$.

The ADC pulse-height signals from each phototube of the shower counter were proportional to the total energy deposited in each block. However, the proportionality constants were different because of the slightly different gains of each phototube. These calibration coefficients were determined using an iterative method of minimizing the shower counter resolution, and normalizing to the E' measured by the magnetic spectrometer. Corrections were made for the effects of light attenuation in the vertical direction within the lead-glass blocks.

A spectrum of normalized shower energy, i.e., the ratio of shower counter energy to the magnetic spectrometer momentum measurement, for the worst case deep inelastic data taken with $\pi/e \approx 125$, for $p = 1.08$ GeV/c, is shown in Fig. 5 with and without the Cherenkov counter threshold cut. The large electron peak at one is clearly seen, along with the low-energy pion tail after the Cherenkov cut is made. By making a cut of normalized shower energy > 0.70, it was possible to achieve π/e discrimination of $\approx$50:1, in addition to the Cherenkov discrimination, while still maintaining an efficiency for electron events of $\geq 99.9\%$. Note that our trigger is biassed against pions, and therefore it is not straightforward to determine a pion rejection factor from Fig. 5 alone. One needs to take into account true π/e rates, which were measured by scalers.

After identifying the electron events and determining the scattering kinematics, the results were accumulated in a three-dimensional histogram $N_e(\Delta p/p, \Delta\theta, \phi)$. The total number of electrons detected in the good acceptance region defined by $-3.5 < \Delta p/p < 3.5\%$, $-6 < \Delta\theta < 6$ mr and $28 < \phi < 28$ mr, was obtained by summing the counts in the event histogram. Small pion contamination, obtained by extrapolating the low shower energy pion tails in Fig. 5 to the region of normalized shower energy > 0.7, was then subtracted to obtain the number of electrons ($N_e^{\rm tot}$) detected in each run. This pion subtraction was always less than 0.2%.

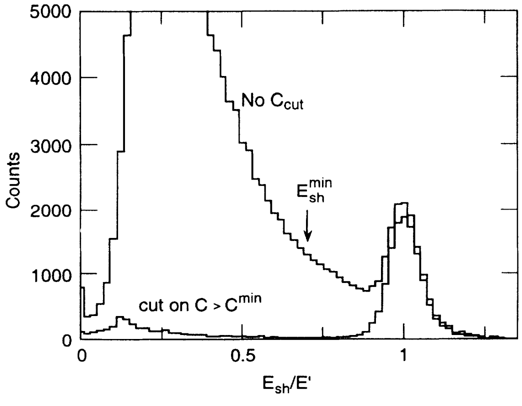

FIG. 5. Normalized shower energy spectrum with and without a cut on the Cherenkov counter pulse height. $E_{\rm sh}^{\rm min} = 0.7$ is the value of shower counter cut used to select electrons in the analysis.

3. Spectrometer momentum and angle corrections

The spectrometer magnetic field was monitored at every setting using a NMR probe. The absolute value of spectrometer momentum setting was determined through floating wire studies. A small correction factor was applied to account for small point-to-point variation. The spectrometer angle setting was also corrected for calibration determined by surveys of the spectrometer before and after the experiment. The spectrometer calibration is discussed in detail in Appendix A.

C. Inelastic cross section calculation

Cross sections were calculated for each (x, Q^2, ϵ) point in the next step of the analysis. The measured "experimental" cross section was given by

$$\frac{d\sigma_{\rm expt}}{d\Omega dE'} = \frac{N_e^{\rm tot}}{Q_e n_t A^{\rm tot} E'} \cdot \frac{C_c C_e C_k C_a}{\epsilon_c \epsilon_w \epsilon_s}, \tag{10}$$

where $N_e^{\rm tot}$ was the total number of electrons detected in solid angle $\Delta\Omega$ with energy between $E' - \Delta E'/2$ and $E' + \Delta E'/2$, Q_e was the number of incident electrons, n_t was the number of target nucleons per unit area, $A^{\rm tot}$ was the total momentum and angular acceptance, and C's and ϵ's were correction factors and efficiencies, respectively. Correction factors were applied for all known effects larger than 0.1%. These corrections were due to computer dead time (C_c), electronics dead time (C_e), kinematic correction (C_k) to adjust the cross section to the nominal (x, Q^2) setting, and variation of cross section within the spectrometer acceptance (C_a), i.e., the bin centering correction. The quantities ϵ_c, ϵ_w, and ϵ_s were efficiencies of Cherenkov counter, wire chambers, and shower counter, respectively. These, and corrections to the deuterium target density (C_H), solid target neutron excess (C_n) are discussed below.

The number of incident electrons (Q_e) was measured by the two independent toroid systems discussed earlier. The average of the two toroid readings, after corrections for any calibration changes, was used in the analysis.

The values for number of nucleons per unit area, n_t, were obtained from target thicknesses listed in Table III. Fits [40] to liquid D and H density measurements were used to obtain the nominal target density. There was a 2% hydrogen atomic contamination in the liquid deuterium target. A correction factor,

$$C_H = \left[1 - 0.0204\left(1 - \frac{1}{1 + \frac{\sigma_n}{\sigma_p}}\right)\right]^{-1}, \tag{11}$$

computed using a σ_n/σ_p fit to previous data [4], was applied to deuterium cross section to correct for this proton excess. The nominal liquid deuterium density was corrected for average changes in density, using the measurements of the target temperature and pressure made during the running. Local nonuniformity due to beam heating was studied in separate data runs as described earlier.

The total acceptance A^{tot} was given by

$$A^{\text{tot}} = A^{\text{nom}} A_p^{\text{corr}} A_L^{\text{corr}}, \tag{12}$$

where $A^{\text{nom}} = \Delta\Omega \Delta E'/E'$ is the sum over the good acceptance region of $A(\Delta p/p, \Delta\theta, \phi)$. The nominal good acceptance A^{nom} was 0.0366 mstr %. The corrections to the nominal acceptance, due to target length for the deuterium target, A_L^{corr}, and due to the spectrometer momentum setting, A_p^{corr}, are discussed in detail in Appendix A. The target length correction A_L^{corr} was less than 0.4% even at the largest angle. The momentum-dependent correction A_p^{corr} was less than 0.3% at the highest momentum.

Within the spectrometer acceptance, the cross sections varied by several percent. A center-of-bin correction factor C_a was used to obtain the cross section at the central setting of the spectrometer. C_a was calculated using a fit to old SLAC data [4], and our data binned in $\Delta p/p$, $\Delta\theta$, and ϕ. The correction factor C_a is given by

$$C_a = \frac{\sigma_F^c \sum A(\Delta p/p, \Delta\theta, \phi)}{\sum \sigma_F(\Delta p/p, \Delta\theta, \phi) A(\Delta p/p, \Delta\theta, \phi)}, \tag{13}$$

where $A(\Delta p/p, \Delta\theta, \phi)$ is the acceptance function (see Appendix A), $\sigma_F(\Delta p/p, \Delta\theta, \phi)$ and σ_F^c are the values of the fit to the "experimental" cross sections in the bins and at the central setting respectively, and the sum runs over $\Delta p/p$, $\Delta\theta$, and ϕ. The original fits for Born cross section [4] were modified by a parametrization of variation of radiative corrections within the spectrometer to obtain the fit to "experimental" cross section.

Kinematic correction (C_k) was applied to correct the cross section for slight offsets in the settings of the spectrometer energy and angle compared to the nominal values, so that all ϵ points had the same (x, Q^2). This correction, obtained using the fit to old SLAC inelastic data [4] was typically 0.5%, and was 2% for the worst case. The error on the cross section due to this correction is estimated to be negligible.

Computer dead time (C_c) was determined in three different ways. The first method was to use scalers to determine the fractional number of PR, TAD, and C coincidences (PTC) missed by the computer. The second method consisted of using the long gate (1.6 μs) ADC histogram for the PTC discriminator pulse. The fraction of times the ADC pulse was higher than the single-event pulse gave the correction to account for the events missed by the computer. The third method was to assume Poisson statistics for events to occur within a beam spill and to estimate probability for multiple events knowing the probability for single-event occurrence. All the methods yielded the same results within errors of 0.2%, and only corrections from the first method were applied to obtain final results. These corrections were a maximum of 18%, and were the biggest correction to the measured cross section.

Electronics dead time (C_e) was also determined using the PTC scalers. The PTC pulses of different gate widths (20, 40, 60, and 80 ns) were counted separately, and these were extrapolated to 0 ns to estimate the corrections for the finite width. These corrections C_e were small, at a maximum of 0.5%.

Efficiency of wire chambers for track reconstruction was determined by comparing the number of good electron tracks reconstructed with potentially good electrons defined by the Cherenkov, shower, and scintillators alone. This efficiency ϵ_w varied between 99.6% and 100%, and was computed run by run and applied to the cross section. The efficiencies of Cherenkov and shower counters were calculated using the data from runs where the pion background was small. A run-by-run calculation of these efficiencies, to the accuracy required, was not possible as it was difficult to identify a clean sample of electrons demanding signals from one of these two counters alone. The efficiencies of the Cherenkov counter ϵ_c and the shower counter ϵ_s with the cuts defined earlier were each 99.7%.

The data were accumulated in many small runs to reduce systematic effects due to any time-dependent fluctuations in incident beam position, angle, energy, charge monitors, detector efficiencies, and duty cycle. The cross sections obtained at similar kinematic setups were then averaged (weighted by the statistical error). The background from processes other than deep inelastic scattering, and in the case of the liquid target the background from scattering off the target end caps, were subtracted.

The flux of electrons from processes other than deep inelastic is dominated by the charge-symmetric processes [41], e.g., π^0 decays. It was determined by reversing spectrometer polarity and measuring positron yeilds, when electrons were incident on the target. Other contributions, in particular noncharge-symmetric decay of charged kaons, were estimated to be negligible. In an

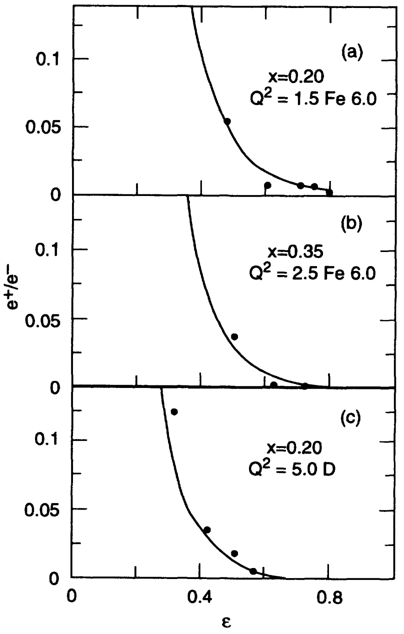

FIG. 6. The ratios of yields e^+/e^- measured in this experiment are plotted versus ϵ, for a sample of (x, Q^2) points. The solid line is a fit e^+/e^- data obtained using data from earlier SLAC experiments. For the few kinematic settings where positron contribution is expected to be small, positron data were not measured in this experiment, and this fit was used for subtraction.

TABLE V. Cross sections (in nb/sr GeV) for all kinematic points and targets. The statistical and point-to-point systematic errors (fractional) are also tabulated. There is an additional normalization uncertainty of $\sim 2\%$. These cross sections have been radiatively corrected. Radiative correction factors which multiply the measured cross sections are also given.

E_0	E'	θ	ϵ	C_r	σ	$\Delta\sigma/\sigma$	
						stat	syst
Deuterium							
x=0.20	Q^2=1.0						
3.748	1.084	28.728	0.485	0.773	3.641×10^4	0.009	0.005
4.006	1.342	24.906	0.559	0.803	4.944×10^4	0.009	0.006
4.251	1.586	22.205	0.616	0.825	6.496×10^4	0.008	0.006
5.507	2.843	14.520	0.792	0.889	1.742×10^5	0.008	0.006
6.251	3.586	12.124	0.845	0.915	2.670×10^5	0.007	0.007
x=0.20	Q^2=1.5						
5.507	1.510	24.519	0.476	0.779	2.267×10^4	0.009	0.005
6.250	2.253	18.783	0.611	0.835	4.039×10^4	0.006	0.006
7.002	3.005	15.343	0.703	0.869	6.489×10^4	0.006	0.006
7.498	3.502	13.727	0.748	0.885	8.467×10^4	0.006	0.006
8.251	4.254	11.866	0.799	0.905	1.189×10^5	0.006	0.006
x=0.20	Q^2=2.5						
8.251	1.589	25.220	0.348	0.721	7.527×10^3	0.014	0.006
10.243	3.582	14.999	0.606	0.850	2.318×10^4	0.004	0.006
11.744	5.083	11.746	0.716	0.889	4.026×10^4	0.007	0.006
x=0.20	Q^2=5.0						
16.005	2.683	19.647	0.314	0.713	2.931×10^3	0.011	0.006
17.255	3.933	15.600	0.422	0.790	4.847×10^3	0.008	0.006
18.491	5.169	13.134	0.508	0.832	7.078×10^3	0.007	0.006
19.493	6.171	11.702	0.566	0.854	9.246×10^3	0.006	0.006
x=0.35	Q^2=1.5						
3.748	1.464	30.304	0.604	0.933	2.266×10^4	0.007	0.006
4.007	1.723	26.950	0.660	0.953	2.946×10^4	0.007	0.006
4.250	1.966	24.459	0.704	0.967	3.644×10^4	0.007	0.006
5.507	3.223	16.715	0.838	1.025	8.795×10^4	0.007	0.006
7.002	4.718	12.232	0.907	1.072	1.785×10^5	0.013	0.007
x=0.35	Q^2=2.5						
5.501	1.695	30.008	0.506	0.914	7.593×10^3	0.008	0.005
6.250	2.443	23.345	0.633	0.959	1.307×10^4	0.007	0.006
7.081	3.274	18.900	0.726	0.994	2.107×10^4	0.007	0.006
7.498	3.692	17.283	0.761	1.008	2.614×10^4	0.006	0.006
9.710	5.904	11.986	0.870	1.062	5.952×10^4	0.007	0.006
x=0.35	Q^2=5.0						
10.243	2.630	24.878	0.449	0.919	2.498×10^3	0.010	0.005
11.753	4.140	18.447	0.601	0.975	4.791×10^3	0.006	0.006
13.320	5.707	14.735	0.704	1.011	8.016×10^3	0.006	0.006
15.004	7.391	12.189	0.777	1.040	1.225×10^4	0.006	0.006
x=0.50	Q^2=2.5						
3.749	1.084	46.177	0.417	0.962	3.011×10^3	0.009	0.006
4.251	1.587	35.447	0.561	1.015	5.309×10^3	0.010	0.006
5.502	2.838	23.082	0.758	1.088	1.375×10^4	0.009	0.006
7.082	4.418	16.250	0.865	1.148	3.062×10^4	0.006	0.006
9.248	6.584	11.630	0.926	1.206	6.363×10^4	0.007	0.006
x=0.50	Q^2=5.0						
7.084	1.755	36.976	0.401	0.985	9.454×10^2	0.013	0.006
8.250	2.921	26.331	0.578	1.050	1.963×10^3	0.007	0.005
9.710	4.381	19.742	0.712	1.099	3.749×10^3	0.007	0.006
13.316	7.987	12.448	0.863	1.179	1.048×10^4	0.005	0.006
x=0.50	Q^2=7.5						
10.243	2.249	33.152	0.372	0.990	4.679×10^2	0.016	0.007
14.991	6.997	15.367	0.743	1.128	2.554×10^3	0.010	0.006
x=0.50	Q^2=10.0						
13.319	2.661	30.802	0.348	0.991	2.918×10^2	0.012	0.007
15.005	4.348	22.578	0.504	1.050	5.580×10^2	0.012	0.006
18.490	7.832	15.100	0.697	1.119	1.351×10^3	0.006	0.006

TABLE V. (*Continued*).

E_0	E'	θ	ϵ	C_r	σ	$\Delta\sigma/\sigma$	
						stat	syst
Fe 6.0							
x=0.20	Q^2=1.0						
3.748	1.084	28.728	0.485	0.741	1.035×10^6	0.013	0.005
4.006	1.342	24.906	0.559	0.777	1.450×10^6	0.009	0.005
4.251	1.586	22.205	0.616	0.804	1.817×10^6	0.012	0.005
5.507	2.843	14.520	0.792	0.886	4.928×10^6	0.008	0.006
6.251	3.586	12.124	0.845	0.918	7.519×10^6	0.007	0.006
x=0.20	Q^2=1.5						
5.507	1.510	24.519	0.476	0.746	6.574×10^5	0.010	0.005
6.250	2.253	18.783	0.611	0.815	1.170×10^6	0.006	0.005
7.002	3.005	15.343	0.703	0.859	1.865×10^6	0.006	0.005
7.498	3.502	13.727	0.748	0.880	2.394×10^6	0.007	0.006
8.251	4.254	11.866	0.799	0.908	3.363×10^6	0.006	0.006
x=0.20	Q^2=2.5						
8.251	1.589	25.220	0.348	0.680	2.050×10^5	0.016	0.006
10.243	3.582	14.999	0.606	0.834	6.624×10^5	0.006	0.005
11.744	5.083	11.746	0.716	0.885	1.151×10^6	0.007	0.006
x=0.35	Q^2=1.5						
3.748	1.464	30.304	0.604	0.955	6.217×10^5	0.010	0.005
4.007	1.723	26.950	0.660	0.980	8.212×10^5	0.008	0.005
4.250	1.966	24.459	0.704	1.000	1.005×10^6	0.008	0.005
5.507	3.223	16.715	0.838	1.073	2.424×10^6	0.008	0.006
7.002	4.718	12.232	0.907	1.132	5.024×10^6	0.012	0.006
x=0.35	Q^2=2.5						
5.501	1.695	30.008	0.506	0.929	2.022×10^5	0.011	0.005
6.250	2.443	23.345	0.633	0.988	3.614×10^5	0.009	0.005
7.081	3.274	18.900	0.726	1.030	5.829×10^5	0.007	0.005
7.498	3.692	17.283	0.761	1.049	7.212×10^5	0.007	0.005
9.710	5.904	11.986	0.870	1.117	1.643×10^5	0.007	0.006
x=0.35	Q^2=5.0						
10.243	2.630	24.878	0.449	0.933	6.712×10^4	0.012	0.005
11.753	4.140	18.447	0.601	1.003	1.305×10^5	0.008	0.005
13.320	5.707	14.735	0.704	1.050	2.166×10^5	0.007	0.005
15.004	7.391	12.189	0.777	1.083	3.332×10^5	0.006	0.005
x=0.50	Q^2=2.5						
3.749	1.084	46.177	0.417	1.011	7.736×10^4	0.011	0.006
4.251	1.587	35.447	0.561	1.073	1.339×10^5	0.010	0.005
5.502	2.838	23.082	0.758	1.163	3.563×10^5	0.011	0.005
7.082	4.418	16.250	0.865	1.235	7.792×10^5	0.007	0.005
9.248	6.584	11.630	0.926	1.307	1.645×10^6	0.007	0.005
x=0.50	Q^2=5.0						
7.084	1.755	36.976	0.401	1.033	2.451×10^4	0.022	0.006
8.250	2.921	26.331	0.578	1.115	5.090×10^4	0.011	0.005
9.710	4.381	19.742	0.712	1.175	9.593×10^4	0.009	0.005
13.316	7.987	12.448	0.863	1.271	2.702×10^4	0.008	0.005
Fe 2.6							
x=0.20	Q^2=1.0						
3.748	1.084	28.728	0.485	0.793	1.020×10^6	0.014	0.005
4.006	1.342	24.906	0.559	0.820	1.393×10^6	0.008	0.005
4.251	1.586	22.205	0.616	0.841	1.821×10^6	0.008	0.005
5.507	2.843	14.520	0.792	0.901	4.865×10^6	0.008	0.006
6.251	3.586	12.124	0.845	0.924	7.430×10^6	0.007	0.006
x=0.50	Q^2=2.5						
3.749	1.084	46.177	0.417	0.991	7.566×10^4	0.007	0.006
9.248	6.584	11.630	0.926	1.196	1.619×10^6	0.018	0.005

TABLE V. (*Continued*).

E_0	E'	θ	ϵ	C_r	σ	$\Delta\sigma/\sigma$	
						stat	syst
Gold							
x=0.20	Q^2=1.0						
3.748	1.084	28.728	0.485	0.753	3.599×10^6	0.014	0.005
4.006	1.342	24.906	0.559	0.787	4.925×10^6	0.009	0.005
4.251	1.586	22.205	0.616	0.814	6.416×10^6	0.007	0.005
5.507	2.843	14.520	0.792	0.893	1.708×10^7	0.008	0.006
6.251	3.586	12.124	0.845	0.925	2.624×10^7	0.006	0.006

earlier experiment [41] positron yields with incident electrons, and electron yields with incident positrons were measured, and were found to be equal within experimental uncertainty. We estimate that the "positron" subtraction accounts for electrons from processes other than deep inelastic scattering to the level of ±5% accuracy. This subtraction was a maximum of 13% for the 6% r.l. iron target at the lowest (x, Q^2, ϵ) kinematic setting, but was typically $< 2\%$. Positron yields were measured at all kinematic settings where the subtraction was greater than 0.5%. Where the positron yield was not measured a subtraction was made using a fit to such positron yields measured in previous experiments at SLAC [4]. Figure 6 shows the ratio of yields e^+/e^- versus ϵ for a sample of x, Q^2 points, along with the fits.

The electron scattering contribution from the aluminum target end caps was determined using an empty target replica. To account for radiative effects as well as to increase the counting rate, additional aluminum was added at the front and the back of the target end caps, to make the total radiation lengths of the replica identical to the deuterium target. This subtraction was 1.2% on average and was determined to 10% accuracy.

The cross section after these subtractions and corrections, includes contributions to the scattering from higher-order electromagnetic processes. The experimental cross sections were divided by the radiative corrections (described in detail in the Appendix B), C_r, to obtain final Born cross sections at each kinematic setting. Methods of Bardin *et al.* [42–44], and an improved method of Mo and Tsai [45,46], were used to calculate the internal radiative corrections. These methods agreed to better than 1%. The external radiative corrections were calculated using complete calculation of Tsai. Experimental tests using radiators of 2.6%, 6%, and 12% r.l. confirmed the calculations to be better than 1%. Table V shows the final cross sections and radiative corrections, for all the kinematic points. Both the statistical and point-to-point systematic errors are shown. The point-to-point error was estimated by feeding in the individual uncertainties in the kinematic variables to the fit to previous SLAC cross section data [4]. Typical contributions to the uncertainty in cross sections are shown in Table II. There is an additional overall normalization uncertainty of 1.7% for the deuterium target, 1.6% for the 6.0% iron target, 1.9% for the 2.6% iron target, and 2.9% for the gold target. Individual contributions to this uncertainty are shown in Table VI.

Iron and gold cross sections were converted to cross section per nucleon by applying a neutron excess correction C_n, given by

$$C_n = \frac{1}{2A}\frac{1+\frac{\sigma_n}{\sigma_p}}{\frac{Z}{A}+\left(1-\frac{Z}{A}\right)\frac{\sigma_n}{\sigma_p}} . \tag{14}$$

The neutron to proton cross section ratio $\sigma_n/\sigma_p(x) = 1 - 0.8x$ was obtained from a fit to previous SLAC data [4]. Z and A are the number of protons and the number of nucleons in the nucleus. These cross sections, used in obtaining R, $R_A - R_D$, and σ_A/σ_D, represent the cross section per nucleon, of a hypothetical nucleus (atomic mass A) with an equal number $(A/2)$ of protons and neutrons.

TABLE VI. Normalization uncertainties (±) are listed, in percentages, for all targets. Solid target neutron excess correction error is relevant only for cross sections per nucleon used in the determination of σ^A/σ^D.

	Deuterium	Iron(6.0%)	Iron(2.6%)	Gold
Incident energy	0.3	0.3	0.3	0.3
Charge measurement	0.5	0.5	0.5	0.5
Target length	0.8	0.5	1.1	2.5
Scattered energy	0.1	0.1	0.1	0.1
Spectrometer angle	0.2	0.2	0.2	0.2
Acceptance	1.0	1.0	1.0	1.0
Rad. corr. ϵ dep.	1.0	1.0	1.0	1.0
Rad. corr. norm. 1.0	1.0	1.0	1.0	
Fe/Au neutron excess	0.0	0.2	0.2	0.4
Total normalization	1.7	1.6	1.9	2.9

IV. RESULTS

A. $R = \sigma_L/\sigma_T$ and F_2 extraction

The values of R and F_2 were extracted from cross sections measured at various values of ϵ at fixed (x, Q^2) by making linear fits to $\Sigma = d^2\sigma/d\Omega dE'/\Gamma$ versus ϵ according to Eq. (2). The values of Σ were weighted by the quadratic sum of statistical and point-to-point systematic errors in making the linear fits. The values of R are insensitive to the absolute normalization of beam flux, target length, and spectrometer acceptance. The fits at each (x, Q^2) point for all targets are shown in Fig. 7. The average $\chi^2/$ per degree of freedom for these fits is 0.7, indicating that the estimate of point-to-point systematic uncertainty is conservative. The fits were also made with only statistical errors on cross sections to find the individual contributions to the error. The values for R and F_2, with statistical and systematic errors, obtained for all (x, Q^2) points and targets are shown in Table VII. In addition to the point-to-point systematic errors, there is an uncertainty of ± 0.03 on R primarily due to errors on radiative corrections correlated with ϵ (see Table II).

The results for R plotted in Figs. 8 and 9 were averaged for different targets at the same x and Q^2, because the values of the differences $R_A - R_D$ are consistent with zero, as discussed below. Our results at x of 0.2, 0.35, and 0.5 show a clear falloff of R with increasing Q^2. The agreement with a constant value of R=0.2 is poor. The high Q^2 results from CDHS [47], BCDMS [48] and EM [49] Collaborations, are also plotted in Fig. 8. These results reinforce our conclusion that R decreases with increasing Q^2. Figure 9 shows R plotted against x, for Q^2 values of 1.5, 2.5, and 5 GeV^2. There is little dependence of R on the variable x in this x range.

1. *Comparisons with theory*

In the naive parton model at very high Q^2, R is expected to be zero. At finite values of Q^2, target mass effects are taken into account naively by the Callan-Gross relation, i.e., $R = 4M^2x^2/Q^2$. This naive view has wrong x dependence as shown by the dot-dashed curve in Fig. 9.

In perturbative QCD, to the order α_s, hard gluon bremsstrahlung from quarks, and photon-gluon interaction effects yield contributions to leptoproduction [8]. The QCD structure functions are given by

$$F_2^{\rm QCD}(x,Q^2) = \sum_i e_i^2 x\left[q_i(x,Q^2) + q_i(x,Q^2)\right], \tag{15}$$

$$F_L^{\rm QCD}(x,Q^2) = \frac{\alpha_s(Q^2)}{2\pi}x^2\left[\int_x^1 \frac{du}{u^3}\left(\frac{8}{3}F_2^{\rm QCD}(u,Q^2) + 4\sum_i e_i^2 uG(u,Q^2)(1-x/u)\right)\right], \tag{16}$$

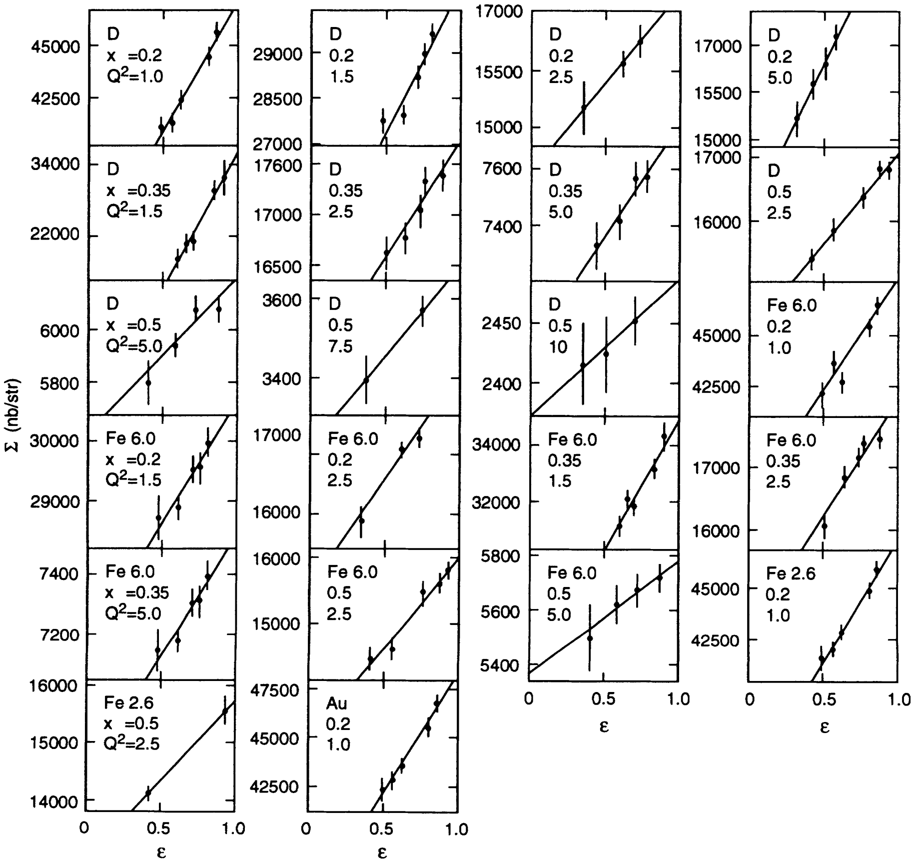

FIG. 7. The Σ vs ϵ fits at each (x, Q^2) point, for every target are shown. The errors on the cross sections include both the statistical and point-to-point systematic errors added in quadrature. The average χ^2 per degree of freedom is 0.7.

TABLE VII. Values of R and F_2 for each (x, Q^2) point and target are tabulated. Statistical and point-to-point systematic errors are shown separately. There is an additional normalization error of 0.03 primarily due to radiative corrections. There is an additional 2% normalization error for F_2.

Target	x	Q^2	$\delta\epsilon$	F_2	ΔF_2(stat)	ΔF_2(syst)	R	ΔR(stat)	ΔR(syst)	$\chi^2/N_{\rm DF}$
D	0.20	1.0	0.36	0.297	0.009	0.007	0.376	0.042	0.031	2.5/3
D	0.20	1.5	0.32	0.299	0.009	0.008	0.269	0.042	0.030	4.6/3
D	0.20	2.5	0.37	0.291	0.016	0.010	0.104	0.047	0.027	0.0/1
D	0.20	5.0	0.25	0.303	0.021	0.016	0.233	0.055	0.040	0.2/2
D	0.35	1.5	0.30	0.232	0.010	0.008	0.296	0.051	0.040	0.9/3
D	0.35	2.5	0.36	0.219	0.008	0.007	0.153	0.033	0.025	2.0/3
D	0.35	5.0	0.33	0.208	0.011	0.009	0.123	0.037	0.028	0.6/2
D	0.50	2.5	0.51	0.141	0.006	0.005	0.202	0.025	0.018	1.1/3
D	0.50	5.0	0.46	0.117	0.007	0.007	0.102	0.026	0.022	1.6/2
D	0.50	7.5	0.37	0.110	0.019	0.011	0.145	0.059	0.029	0.0/0
D	0.50	10.0	0.35	0.102	0.015	0.013	0.046	0.038	0.028	0.0/1
Fe 6.0	0.20	1.0	0.36	0.299	0.009	0.007	0.298	0.043	0.027	5.3/3
Fe 6.0	0.20	1.5	0.32	0.299	0.010	0.008	0.158	0.038	0.027	1.7/3
Fe 6.0	0.20	2.5	0.37	0.310	0.016	0.010	0.254	0.058	0.033	1.2/1
Fe 6.0	0.35	1.5	0.30	0.235	0.011	0.007	0.348	0.062	0.038	3.4/3
Fe 6.0	0.35	2.5	0.36	0.223	0.009	0.006	0.257	0.044	0.029	3.6/3
Fe 6.0	0.35	5.0	0.33	0.205	0.012	0.008	0.148	0.044	0.026	0.1/2
Fe 6.0	0.50	2.5	0.51	0.132	0.006	0.004	0.226	0.029	0.017	2.0/3
Fe 6.0	0.50	5.0	0.46	0.109	0.011	0.006	0.078	0.042	0.020	0.2/2
Fe 2.6	0.20	1.0	0.36	0.297	0.009	0.007	0.357	0.045	0.030	0.9/3
Fe 2.6	0.50	2.5	0.51	0.130	0.020	0.006	0.223	0.050	0.020	0.0/0
Au	0.20	1.0	0.36	0.301	0.008	0.007	0.352	0.043	0.030	1.7/3

$$2xF_1^{\rm QCD}(x,Q^2) = F_2^{\rm QCD} - F_L^{\rm QCD}, \tag{17}$$

and

$$R^{\rm QCD}(x,Q^2) = \frac{F_L^{\rm QCD}}{2xF_1^{\rm QCD}}, \tag{18}$$

where

$$\alpha_s(Q^2) = \frac{12\pi}{(33-n_f)\ln[Q^2/\Lambda^2(n_f)]}, \tag{19}$$

$$n_f = 3 \quad \text{for} \quad Q^2 < m_c^2, \tag{20}$$

$$n_f = 4 \quad \text{for} \quad m_c^2 \le Q^2 < m_b^2, \tag{21}$$

$$n_f = 5 \quad \text{for} \quad Q^2 \ge m_b^2. \tag{22}$$

The quark masses used are $m_c = 1.35$ GeV, and $m_b = 4.25$ GeV. The first and second terms in the integrand for $F_L^{\rm QCD}$ [see Eq. (16)] correspond to the hard gluon bremsstrahlung and photon-gluon interaction effects, respectively. The leading Q^2 dependence of the structure functions is in α_s, and is therefore logarithmic. In this calculation of F_L all kinematic terms of the order M^2/Q^2 were ignored. The calculation of QCD contributions to structure functions requires the knowledge of primordial quark $[q_i(x,Q^2)]$ and gluon $[G(x,Q^2)]$ distribution functions. The quark and gluon x distributions are extracted from muon-nucleon and neutrino-nucleon scattering data at a particular $Q^2 = Q_0^2$. Perturbative QCD enables calculation of quark and gluon momentum distributions at other Q^2 values using Altarelli-Parisi equations [50]. The Q^2 evolution of these distributions has been parametrized by various groups [51–56]. These fits were strictly valid only for $Q^2 > Q_0^2$, where the values of Q_0^2 varied between 4 and 5 GeV^2. However, the Q^2 dependence of the distributions was smooth, so we have extrapolated the distributions below the nominal Q^2 logarithmically. The values of Λ and the order of α for each fit was the same as was used in the extraction of quark distributions. This value $\Lambda(n_f)$ was changed when the quark mass thresholds are crossed such that $\alpha_s(Q^2)$ is continuous. The Martin-Roberts-Stirling set D (MRS-D) distributions [55] are found to provide best fit to the very high Q^2 and low x data from the DESY ep collider HERA.

As shown by the lightly hashed bands in Figs. 8 and 9, our data on R are not in agreement, except at low x, with this perturbative QCD calculation made using various quark distributions. Target mass and higher twist effects need to be included as discussed below. These QCD contributions to R calculated using various sets of quark distributions differ quite substantially at $x = 0.2$, and are compared to our data in Fig. 10. The uncertainty in the gluon distribution function is responsible for these differences. Note that Morfin-Tong (MT) [53] and MRS [54,55] structure functions use the latest data on deep inelastic scattering.

The kinematic effects due to target mass dominate at small Q^2 and large x. These effects were first calculated

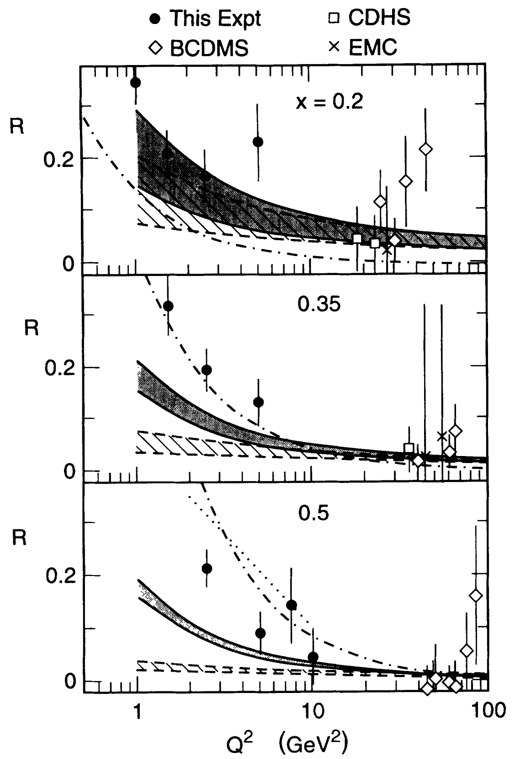

FIG. 8. The values of R at different x (0.2, 0.35, and 0.5), averaged over all targets, are plotted versus Q^2, with all statistical and point-to-point systematic errors added in quadrature. The data from high Q^2 CDHS (ν-Fe), EMC (μ-D), and BCDMS (μ-C/H) experiments are also plotted. The lower lightly hashed band is the range of perturbative QCD predictions for R obtained using various standard quark-gluon distribution functions. The higher boldly hashed band is similarly computed range for QCD including target mass effects. The dot-dashed line is the prediction of the naive parton model. The dotted line for x=0.5 is the prediction of a diquark model.

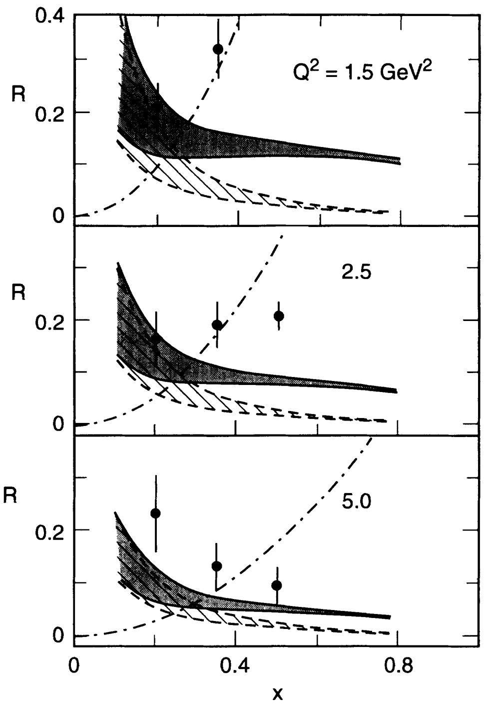

FIG. 9. The values of R at Q^2=1.5, 2.5, and 5 GeV^2 are plotted against x. The errors shown include all statistical and point-to-point systematic errors added in quadrature. The lower lightly hashed band is the range of perturbative QCD predictions for R obtained using various standard quark-gluon distribution functions. The higher boldly hashed band is similarly computed range for QCD including target mass effects. The dot-dashed line is the prediction of the naive parton model.

in the framework of operator product expansion and moment analysis [9] by Georgi and Politzer (GP). The structure functions including these GP target-mass effects are given by

$$2F_1^{\rm QTM}(x,Q^2) = \frac{1}{k}\frac{2xF_1^{\rm QCD}(\xi,Q^2)}{\xi} + \frac{2M^2}{Q^2}\frac{x^2}{k^2}I_1 + \frac{4M^4}{Q^4}\frac{x^3}{k^3}I_2, \qquad (23)$$

$$F_2^{\rm QTM}(x,Q^2) = \frac{x^2}{k^3}\frac{F_2^{\rm QCD}(\xi,Q^2)}{\xi^2} + \frac{6M^2}{Q^2}\frac{x^3}{k^4}I_1 + \frac{12M^4}{Q^4}\frac{x^4}{k^5}I_2, \qquad (24)$$

and

$$R^{\rm QTM}(x,Q^2) = \frac{F_2^{\rm QTM}}{2xF_1^{\rm QTM}}k^2 - 1, \qquad (25)$$

where

$$k = \left(1 + \frac{4x^2M^2}{Q^2}\right)^{1/2}, \qquad (26)$$

$$\xi = \frac{2x}{1+k}, \qquad (27)$$

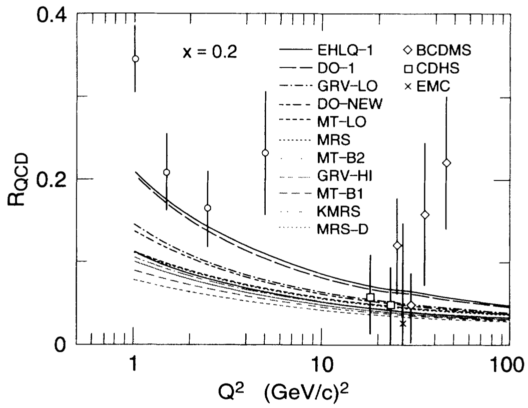

FIG. 10. Our values of R at x = 0.2, plotted versus Q^2, are compared with QCD calculations performed using various standard quark-gluon distribution functions. The quark-gluon distributions are obtained from CERN program library PDFLIB and are labeled as in Ref. [56]. The higher Q^2 data points are from CERN neutrino and muon scattering experiments.

$$I_1 = \int_\xi^1 du \frac{F_2^{\rm QCD}(u,Q^2)}{u^2}, \tag{28}$$

and

$$I_2 = \int_\xi^1 du \int_u^1 dv \frac{F_2^{\rm QCD}(v,Q^2)}{v^2}. \tag{29}$$

Note that the target-mass effects (ξ scaling) introduce M^2/Q^2 terms. The calculations based on this QCD theory including the GP target-mass effects made with various parametrizations of the quark distributions are shown as a boldly hashed band in Figs. 8, 9, and 11. The target-mass effects increase R significantly at high x and low Q^2. The decrease of R with Q^2 and the weak x dependence of R, observed in our data, are in agreement with the $R^{\rm QTM}$ predictions, but the data are systematically higher than the predictions, indicating that there are additional contributions in this kinematic range. The differences between various quark distributions are noticeable at small x. The latest set of quark distributions, MRS-D [55], lies in the middle of the range.

There are several suggestions that at low Q^2 other nonperturbative effects are significant. There is no complete theoretical treatment of these phenomena but there have been several QCD inspired estimates. Some of these higher twist effects, including the target-mass and QCD contributions, were estimated recently [14]. However, these predictions are valid only for large x.

Alternately, it has been proposed [7] that nonperturbative effects such as those due to tightly bound spin-0 diquarks ($M_D^2 = 10$ GeV^2) in nuclei dominate for $1 \le Q^2 \le 10$ GeV^2. These effects are intertwined with quark-gluon interaction effects at low x ($x \le 0.4$), but are measurable at large x. Our measurements at x=0.5 are smaller than the predictions as shown by the dotted curve in Fig. 8 [7].

2. Reanalysis of SLAC data

Precise understanding of the cross section normalizations due to the detailed study of spectrometer acceptance, and improvements in the radiative corrections calculation procedure prompted a reanalysis [26,27] of all previous SLAC data [1–5,17,18]. The reanalysis procedure involved cross-normalizing several experiments, establishing systematic errors for each experiment from archival data, correcting the data for radiative effects using our procedure, and then performing combined fits to the data [28]. Figure 12 shows the values of R obtained by this global analysis plotted versus x, at several values of Q^2. These results reconfirm our earlier assertion that QCD calculations including the target-mass corrections (hatched area in Fig. 12) still fall short of the R data at large x, and they can be explained by a modest contribution from the higher twist effects. At small x the results are in better agreement with structure functions with large gluon distribution. The reanalysis has also yielded F_2 results with improved kinematic range, and has established a low Q^2 normalization for higher-energy muon experiments. These data are consistent with BCDMS [48] and the New Muon Collaboration (NMC) [57] data and are inconsistent with EMC [49] data.

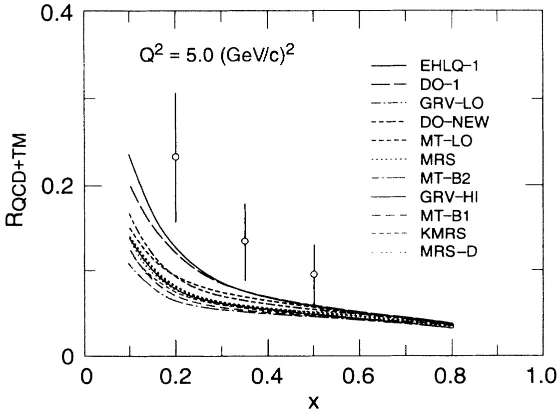

FIG. 11. Our values of R are compared with QCD calculations including target-mass corrections. Various curves are computed using different quark-gluon distribution functions. The quark-gluon distributions are obtained from CERN program library PDFLIB and are labeled as in Ref. [56].

B. $R_A - R_D$ and σ_A/σ_D extraction

The difference $R_A - R_D$ was determined by making linear fits, weighted by the statistical and point-to-point systematic errors, to the ratio of cross sections:

$$\frac{\sigma_A}{\sigma_D} = \frac{\sigma_A^T}{\sigma_D^T}\left[1 + \epsilon'(R_A - R_D)\right] \tag{30}$$

versus $\epsilon' = \epsilon/(1+\epsilon R_D)$. Note that ϵR_D is small, and, therefore, $R_A - R_D$ results are independent of absolute normalizations of spectrometer acceptance, beam intensity, and energy scale. They are also insensitive to the value of R_D, target length, changes in acceptance with ϵ, offsets in beam energy, spectrometer angle, survey errors, long-term charge monitor drifts, and "internal" radiative corrections (see Table II). The fits made at different kinematic points are shown in Fig. 13. The values of $R_A - R_D$ for all (x, Q^2) points are shown in Table VIII. The average χ^2 per degree of freedom for the goodness of fit was 0.7 indicating that the estimate of systematic uncertainty is conservative. The results are also plotted against x for various Q^2 values in Fig. 14. The average $R_A - R_D$ is 0.001±0.018(stat)±0.016(syst), with $\chi^2/N_{\rm DF}$ for agreement with no difference equal to 1.3. The single measurement for Au is consistent with Fe results.

The $R_A - R_D$ results are consistent with zero, in agreement with models predicting no significant A dependence of R in our kinematic range $x \ge 0.2$ (e.g., QCD). We rule out models predicting a large difference $R_A - R_D$, and, in particular, the speculation that the impulse approximation fails. Our data indicate that possible contributions to R from nuclear higher twist effects and possible spin-0 constituents in nuclei are not different from those in nucleons. The σ_A/σ_D measurements are equal to the structure function ratios F_{2A}/F_{2D} and F_{1A}/F_{1D} in the region $0.2 \le x \le 0.5$ [see Eq. (6)].

The results for the ratio σ_A/σ_D averaged over various ϵ

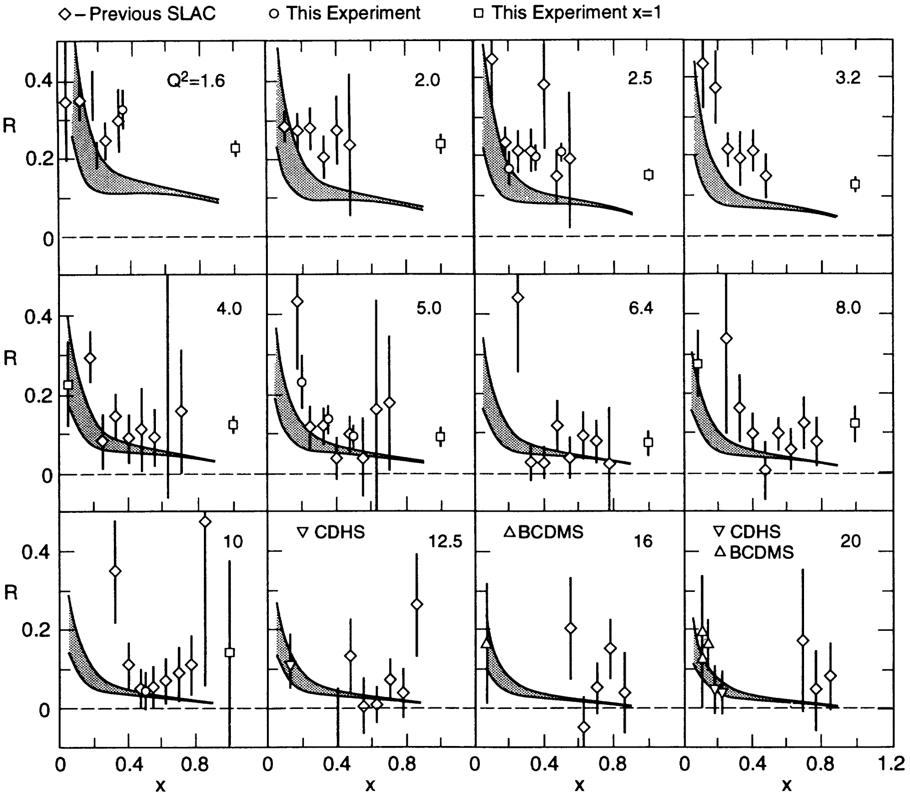

FIG. 12. The values of R, extracted from all previous SLAC data (open diamonds), from inelastic data of this experiment (open circles), and from elastic data of this experiment (open squares), at several values of Q^2, are plotted against x. The errors shown include all statistical and point-to-point systematic errors added in quadrature. The higher Q^2 plots also include data from BCDMS and CDHS. The boldly hashed area is the range of QCD calculations including target-mass effects.

points at each (x, Q^2) are also shown in Table VIII. The overall normalization error (Δ) in σ_A/σ_D of $\Delta = \pm 1.1\%$ is dominated by the errors in target length measurement and radiative corrections. In the averaging, many point-to-point systematic errors are reduced by $1/\sqrt{N_\epsilon}$, where N_ϵ is the number of ϵ points. Figure 15 shows our results for $\sigma_{\mathrm{Fe}}/\sigma_{\mathrm{D}}$ averaged over Q^2 and ϵ compared to the data from SLAC-E139 (with our improved radiative corrections discussed in Appendix B; $\Delta = \pm 1.3\%$) [58], SLAC-E87 ($\Delta = \pm 1.1\%$) [16], and SLAC-E61 ($\Delta = \pm 4.2\%$) [18]. There is excellent agreement among all sets of SLAC data. In Fig. 15 our data are also compared with high-Q^2 data from CERN muon experiments BCDMS ($\Delta = \pm 1.5\%$), and EMC ($\Delta = \pm 0.8\%$) [15]. The lower Q^2 SLAC results are in reasonable agreement with these high-Q^2 muon scattering results, indicating that any Q^2

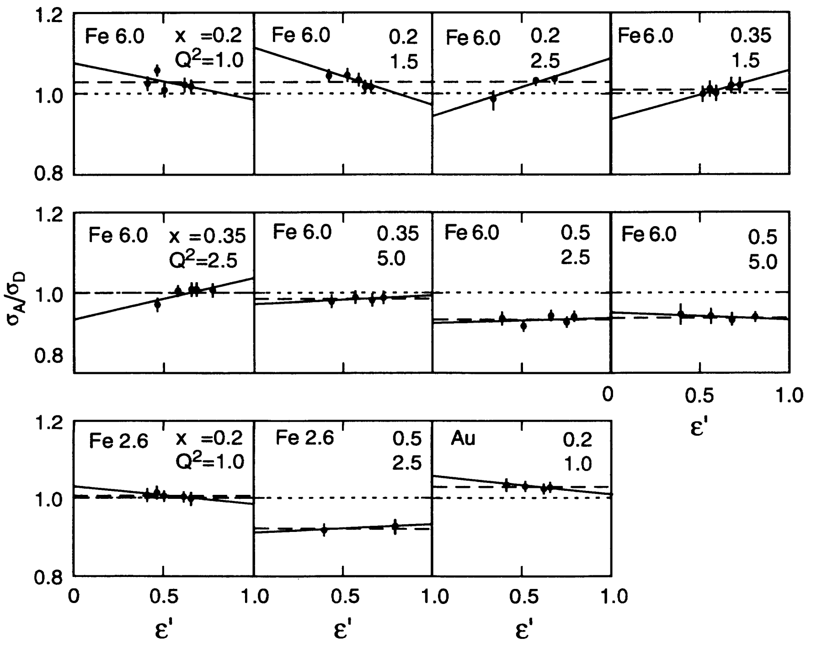

FIG. 13. The fits to the differential cross section ratio σ_A/σ_D versus $\epsilon' = \epsilon/(1 + R^D)$ are shown for each (x, Q^2) point. The errors on the cross section include statistical and point-to-point systematic contributions added in quadrature.

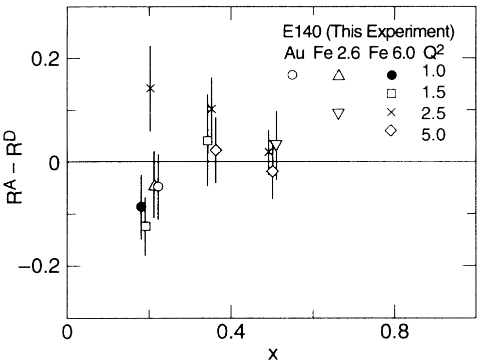

FIG. 14. The results for $R_A - R_D$ averaged over ϵ are plotted as a function of x for each Q^2 and target. Statistical and systematic errors are added in quadrature.

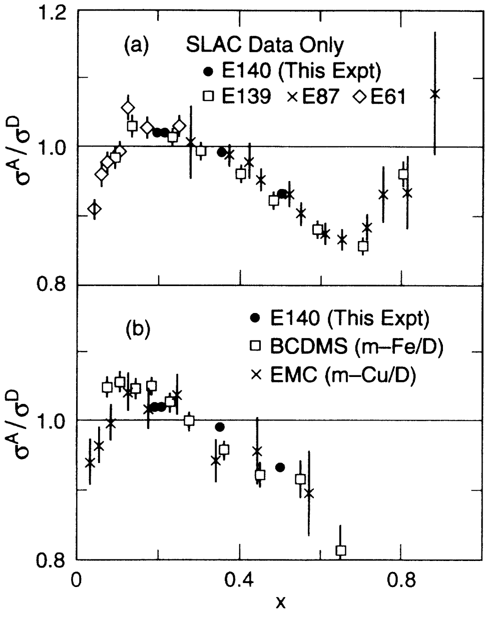

FIG. 15. The results for σ_A/σ_D are plotted as a function of x and are compared to other (a) electron and (b) muon experiments. Our data from Fe and Au are each averaged over ϵ and Q^2. Statistical and point-to-point systematic errors are added in quadrature. There is an additional overall normalization of 1.1%.

dependence of EMC effect must be small. All experiments show a small rise in $\sigma_{\rm Fe}/\sigma_{\rm D}$ for $x \sim 0.2$, but the rise is not as large as in the origninal EMC data [15]. Detailed comparisons of the EMC effect results, including comparisons of SLAC data to NMC, BCDMS, and EMC data and theory, is reported elsewhere [58].

V. CONCLUSIONS

We report on results for the following quantities: the ratio $R = \sigma_L/\sigma_T$ of longitudinal (σ_L) and transverse (σ_T) virtual photon absorption cross sections, the structure functions F_1 and F_2, the differences $R_A - R_D$, and the cross section ratios σ_A/σ_D, measured in deep inelastic electron scattering from targets of deuterium, iron, and gold.

The results for R obtained at x=0.2, 0.35, and 0.5 show a clear falloff with Q^2, in the range $1 \leq Q^2 \leq 10$ GeV^2. The x and Q^2 dependence of the quantity R is inconsistent with the naive parton model, and with the perturbative quantum chromodynamics predictions. Even when effects due to target mass, calculated by Georgi and Politzer (GP), are included the perturbative QCD calculations are somewhat lower than the data. Modest contributions of higher twist terms are necessary to account for this excess over the target-mass-corrected QCD calculations.

This precision experiment as well as our improvements to radiative corrections have been used to renormalize all previous SLAC inelastic data. The results for R in this enhanced kinematic range reconfirm our assertions that small higher twist contributions are needed, in addition to target-mass-corrected QCD. The F_2 results from this reanalysis have established a low Q^2 normalization for the higher-energy muon scattering experiments.

The results on the differences $R_A - R_D$ are consistent with zero, and are in agreement with most models for the EMC effect, including those based on quantum chromodynamics, which predict negligible difference. These results also indicate that there are no significant spin-0 constituents or higher twist effects in nuclei as compared to free nucleons. The measurements of the ratio σ_A/σ_D can now be identified with the structure function ratios F_{2A}/F_{2D} and F_{1A}/F_{1D} unambiguously in our kinematic

TABLE VIII. Values of $R_A - R_D$ and σ_A/σ_D averaged over ϵ with statistical and point-to-point systematic errors. There is an overall normalization of 1.1% in σ^A/σ^D.

Target	x	Q^2	$\delta\epsilon'$	$R^A - R^D$	$\Delta R^A - R^D$(stat)	$\Delta R^A - R^D$(syst)	$\chi^2/N_{\rm DF}$	σ^A/σ^D	$\Delta(\sigma^A/\sigma^D)$(stat)	$\Delta(\sigma^A/\sigma^D)$(syst)
Fe 6.0	0.20	1.0	0.23	-0.086	0.057	0.022	5.6/3	1.021	0.006	0.002
Fe 6.0	0.20	1.5	0.24	-0.124	0.051	0.023	1.3/3	1.028	0.004	0.002
Fe 6.0	0.20	2.5	0.33	0.144	0.079	0.027	1.0/1	1.022	0.006	0.003
Fe 6.0	0.35	1.5	0.20	0.042	0.082	0.033	1.6/3	1.000	0.005	0.002
Fe 6.0	0.35	2.5	0.30	0.102	0.058	0.025	2.8/3	0.993	0.005	0.002
Fe 6.0	0.35	5.0	0.28	0.024	0.058	0.025	0.5/2	0.980	0.005	0.003
Fe 6.0	0.50	2.5	0.40	0.021	0.038	0.016	2.5/3	0.932	0.005	0.002
Fe 6.0	0.50	5.0	0.41	-0.017	0.050	0.020	0.5/2	0.937	0.006	0.003
Fe 2.6	0.20	1.0	0.23	-0.043	0.059	0.024	0.2/3	1.006	0.005	0.002
Fe 2.6	0.50	2.5	0.40	0.033	0.062	0.019	0.0/0	0.917	0.009	0.004
Au	0.20	1.0	0.23	-0.047	0.058	0.024	0.3/3	1.019	0.005	0.002

range ($0.2 \leq x \leq 0.5$ and $1 \leq Q^2 \leq 5$ GeV^2).

The EMC effect, i.e., the x dependence of the ratio F_{2A}/F_{2D}, is confirmed with very small errors and all data (electron and muon scattering) are now in agreement. This ratio is larger than unity in $x \sim 0.2$, and is therefore inconsistent with models using nuclear binding corrections alone to explain EMC effect. Because the ratio F_{2A}/F_{2D} is equal to the ratio of quark distribution functions, we conclude that the EMC effect is due to a nontrivial difference in the quark distribution functions between heavy nuclei and deuteron. This is in agreement with QCD based models, and some convolution models.

ACKNOWLEDGMENTS

We would like to thank the SLAC management and staff, in particular, R. Eisele, C. Hudspeth, G. Davis, J. Mark, M. Starek, and J. Nicol, for their able assistance during the running of this experiment. This research was supported by National Science Foundation Grant Nos. PHY85-05682 and PHY84-10549 and Department of Energy Contract Nos. DE-AC02-76ER13065, DE-AC02-76ER02853, DE-AC03-76SF00515, W-7405-ENG-48, and the US-Israel Binational Science Foundation.

APPENDIX A: CALIBRATION AND ACCEPTANCE OF THE 8 GeV SPECTROMETER

Optical properties of the 8 GeV spectrometer have been extensively studied in the past [38,33,59]. Only the new results relevant to the analysis of this experiment, and, in particular, the results of our recent floating wire calibration study [60,28] of the 8 GeV spectrometer are discussed here.

1. Calibration of the 8 GeV spectrometer

The central scattering angle of the spectrometer [28,60] is calibrated relative to the nominal incident beam line to an accuracy of ±0.006°. This uncertainty includes contributions due to survey errors (±0.001°), uncertainties in the nominal beam line (±0.001°), effects originating in the noncentral rotation of the spectrometer (±0.002°), and uncertainties in the wirefloat determination of the optical axis of the spectrometer relative to its own physical axis (±0.004°). The wirefloat survey study determined an offset of −0.010°, which has been corrected in the analysis. In addition, there is a random uncertainty of ±0.004° in setting the spectrometer.

A correction to the nominal central momentum of the spectrometer, up to 0.2%, was determined by measuring the magnetic fields using an NMR, and was applied in the analysis [60]. An NMR measurement of the field was made for every setting of the spectrometer. Care was taken to de-Gauss the spectrometer properly when changing the spectrometer momentum settings. The central momentum was calibrated to ±0.03% by the wirefloat study [60]. Statistical fluctuations in the computer controlled magnet currents contributed an additional ±0.05% uncertainty.

2. Acceptance of the 8 GeV spectrometer

The acceptance of the spectrometer within the region, $-3.5 < \Delta p/p < 3.5\%$, $-6 < \Delta\theta < 6$ mr, and $-28 < \phi < 28$ mr, was partially limited by collimators, and detector sizes. However, within the fiducial region of $-1 < \Delta p/p < 1\%$, $-2 < \Delta\theta < 2$ mr, and $-10 < \phi < 10$ mr, the acceptance was found to be solely determined by the spectrometer optical properties. The nominal acceptance factor A_{nom} which corrected for the drop in efficiency at the edges of the acceptance was determined using the transport coefficients in Table IV, and solid target inelastic data collected over all the kinematic points in this experiment. Transport coefficients used were determined in 1967 using a dark current electron beam from the accelerator with the spectrometer set at an angle of 0° with respect to the beam axis [61]. These dark current measurements were performed at several energies of the beam. We have reanalyzed these sets of data, and have used the average coefficients obtained using 6 and 8 GeV data sets. There was no significant momentum dependence of these coefficients within the uncertainties of those measurements. Since extraction of R is very sensitive to any kinematics dependent systematic errors, the transport coefficients were measured to high precision in a wirefloat study carried out after this experiment [60]. These wirefloat measurements were used to obtain both absolute calibration of the acceptance and momentum dependence of these optics coefficients. Scattering angle dependence of the nominal acceptance for long targets was studied using a Monte Carlo program.

a. Determination of acceptance function

The acceptance function was generated from the deep inelastic data from this experiment. Trajectories of electrons that scattered off the Fe target, at a variety of kinematic settings, were kinematically reconstructed using the transport coefficients in Table IV, and binned in histograms of $\Delta p/p$, $\Delta\theta$, and ϕ. The expected distribution of events across the acceptance was generated for each kinematic setting from a fit to "experimental" cross sections. To obtain an "experimental" cross section, we corrected the fit to Born cross sections, reported by the previous deep inelastic scattering data [4], for the Fermi motion of the nucleons, the expected value of $R = \sigma_L/\sigma_T$, the EMC effect, radiative corrections, and charge-symmetric backgrounds. A histogram of the expected number of counts in each bin $[N_e^F(\Delta p/p, \Delta\theta, \phi)]$ was generated from this model and was normalized to the measured histogram $[N_e(\Delta p/p, \Delta\theta, \phi)]$ in the central region of the acceptance where the efficiency was expected, based on Monte Carlo studies, to be equal to unity. The normalized model is accurate to better than 1% within the spectrometer acceptance because, in our kinematic domain, the structure functions change little, over the small angle and momentum range of the experiment. Runs in which the cross section had a strong kinematic dependence across the acceptance or large background contributions were excluded. Both of these histograms were then summed over all runs. Averaging over many kinematic points reduce the uncertainty to $< 0.3\%$. A total of $\sim 10^6$ events were included in this analysis. By comparing the two histograms, $N_e^F(\Delta p/p, \Delta\theta, \phi)$ and $N_e(\Delta p/p, \Delta\theta, \phi)$, summed over all runs, the efficiency of each bin could be determined. The acceptance function was thus defined as

$$A(\Delta p/p, \Delta\theta, \phi) = \frac{N_e(\Delta p/p, \Delta\theta, \phi)}{N_e^F(\Delta p/p, \Delta\theta, \phi)}. \qquad \text{(A1)}$$

From this acceptance function it was determined that data would be included only from the region $-3.5 < \Delta p/p < 3.5\%$, $-6 < \Delta\theta < 6$ mr, and $-28 < \phi < 28$ mr. The one-dimensional projection of the acceptance function versus each of these three variables, with these cuts applied, is shown in Fig. 16. The small dip in the θ plot is due to NMR probe obscuring part of the acceptance. The nominal acceptance of the spectrometer A_{nom} in this region was 0.0366 mstr %.

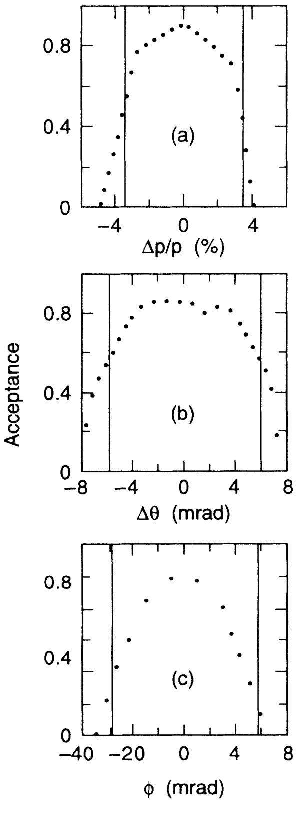

FIG. 16. The acceptance function is plotted versus $\Delta p/p$, $\Delta\theta$, and ϕ, summed over all other bins. The vertical lines indicate the nominal acceptance window in each variable.

b. Momentum dependence

The wirefloat study [60] measured all primary first-order optics coefficients as a function of spectrometer momentum, p. However, these coefficients were not available before the reconstruction of all our data. Therefore, these new coefficients were used to calculate a correction factor A_p^{corr} to the nominal acceptance of the spectrometer, and were applied to our data in the final stage of analysis. The correction factor, including a small correction to the absolute value of the acceptance, is parametrized by

$$A_p^{\text{corr}} = 0.9815 - 0.000\,49(p - 4), \qquad \text{(A2)}$$

where 4 GeV is the weighted mean momentum setting of our data. The uncertainty in this slope is ± 0.0004 GeV^{-1}. The systematic uncertainty of the acceptance is $\pm 1\%$, and it is dominated by spectrometer survey uncertainties.

c. Target length effect

Angle dependence of the acceptance was not anticipated for a zero-length target, based on the surveys of the stability of the spectrometer magnets as the spectrometer was rotated in angle. However, such an effect for an extended target was not ruled out, since events that are initiated from the target ends have a reduced efficiency for reaching the target hut, when the spectrometer is placed at large angles. To determine corrections for this effect, acceptance was studied for the long target as a function of angle using a Monte Carlo simulation of the spectrometer optics. The average of 6 and 8 GeV forward transport coefficients (see Table IV) were used in this simulation. One million events generated with uniform illumination of the spectrometer front window were transported to the spectrometer hut, through all the apertures of the spectrometer, when it was set at $0^\circ - 50^\circ$. The total acceptance was determined for each of the angle settings. A linear fit to the correction of the form

$$A^L_{\text{corr}} = 1 - 2 \times 10^{-5}(L\sin\theta)^2, \qquad \text{(A3)}$$

where $L \sim 20$ cm is the length of the target, fitted the data well. This correction factor applied to the cross section was a maximum of 0.4% at the highest angle of 46°. The target length effect was also studied with all the inelastic data taken from the deuterium target, in a procedure similar to the one used for obtaining the acceptance function described above. Within the errors of that measurement it agreed with the Monte Carlo prediction. The systematic error on the cross section due to this correction is estimated to be below 0.1% level at this highest angle.

APPENDIX B: RADIATIVE CORRECTIONS

Cross sections measured in deep inelastic scattering experiments have large contributions (up to 30% for our data) from processes other than the Born diagram. However, these contributions are dominated by higher-order lepton-photon interactions and are calculable in the theory of quantum electrodynamics. The cross section for the lepton-nucleon inclusive reaction, i.e., where only the scattered electron is detected, to the order α^3 in fine structure constant, are given by the Feynman diagrams as shown in Fig. 17. The differential cross sections for these "internal" processes can be expressed in terms of the electromagnetic structure functions F_1 and F_2 [62]. In addition, the soft multiple photon emission process shown in Fig. 18 is also important at low Q^2. Corrections due to γ-Z interference and hadronic radiation are not discussed in detail here, as they are small in our kinematic range. However, these effects are included in the procedure that was used. For the case of electron scattering, there are also "external" effects, due to low momentum transfer bremsstrahlung and ionization reactions, in the process of electron traversal through the target material (see Fig. 19).

The radiative correction factor C_r, given by $\sigma_{\mathrm{Born}}/\sigma_{\mathrm{rad}}^{i+e}$, where σ_{Born} is the cross section due to the Born diagram and $\sigma_{\mathrm{rad}}^{i+e}$ is the cross section due to the sum of all higher-order diagrams in Figs. 17–19. $\sigma_{\mathrm{rad}}^{i+e}$ can be symbolically expressed as

$$\sigma_{\mathrm{rad}}^{i+e} = \text{external} \otimes \text{internal} \otimes \text{Born}. \qquad \text{(B1)}$$

The convolution program involves integrating over the "internal" and "external" bremsstrahlung photon momenta and angles, and the target dimensions. The integral over the photon momenta require the knowledge of the structure functions F_1 and F_2 over the entire kinematic domain from elastic threshold up to the kinematic point being calculated (see Fig. 20). For ease of parametrization this range is divided into elastic, quasielastic, resonance, and deep inelastic regions. The model Born cross sections used in these calculations were obtained by using fits to previous deep inelastic structure function measurements made at SLAC [4], and fits to global data on nucleon elastic form factors [63]. For nuclear targets (Fe and Au), we have used nuclear elastic form factors [18]. The quasielastic cross section was obtained by smearing the nucleon form factor using a simple fit to the quasielastic peak. The percentage deviations from unity of the radiative to Born cross section ratio for these regions are represented by $\delta_{\mathrm{inel}}, \delta_{\mathrm{qel}}$, and δ_{el}.

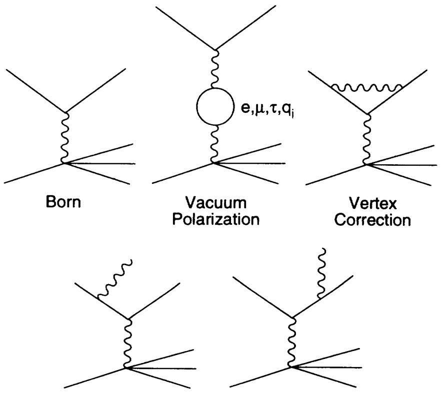

FIG. 17. Feynman diagrams of Born and higher-order radiative corrections which were included in both BARDIN and MTEXACT procedures for internal correction.

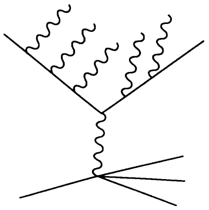

FIG. 18. The soft multiple photon emission process diagram.

It is not practical to exactly compute the multidimensional radiative correction integral represented by Eq. (B1). The "internal" part of the radiative cross section can be computed "exactly" to the one-loop level. However, in the past, in computing the complete multidimensional integral, various degrees of approximation have been made, with corresponding losses in precision. These approximation techniques [45,46] exploit the fact that the bremsstrahlung photons are collinear to the initial and final electrons, and are called angle peaking aproximations. One previously popular method [45,46] involved simultaneous evaluation of both "internal" and "external" contributions by assuming "internal" contribution to be represented by an additional radiator. Further reduction in complexity of the integrals was achieved by "energy" peaking approximation, which enables separation of the incident and scattered electron bremsstrahlung integrals (see Fig. 20). Instead, we have chosen to compute the "internal" radiative cross section "exactly," and add in "external" contributions computed with as few approximations as possible, i.e.,

$$\sigma_{\mathrm{rad}}^{i+e} = \frac{\sigma_{\mathrm{rad}}^{i+e}(\text{approximate})}{\sigma_{\mathrm{rad}}^{i}(\text{approximate})}\sigma_{\mathrm{rad}}^{i}(\text{exact}), \qquad \text{(B2)}$$

and the approximation mostly cancelled in the ratio.

There are two distinct prescriptions for evaluating the "internal" cross sections "exactly," one due to Bardin *et al.* [42–44], and, the other due to Mo and Tsai [45,46]. These prescriptions differ in the way the infrared divergences are tamed. Since the radiative correction errors could significantly effect our results we have undertaken an extensive program to study these different methods and approximation techniques.

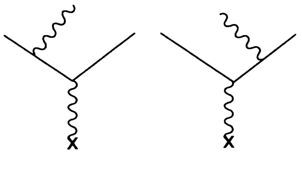

FIG. 19. The external bremsstrahlung diagram.

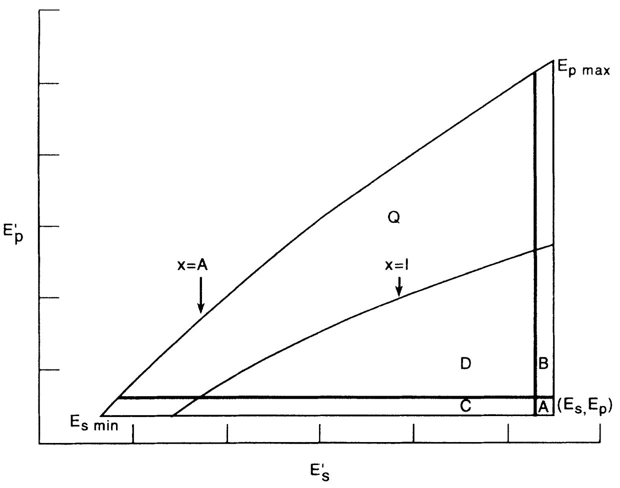

FIG. 20. Radiative correction triangle showing various kinematic regions over which integrals needed to be performed. $x = A$ is the line of elastic scattering from the nucleus, Q is the region of quasielastic scattering from the nucleon, $x = 1$ is the line of elastic scattering from the nucleus, and A, B, C, D are the regions of inelastic scattering. Some approximations were made in evaluating integrals in the regions A, B, and C, in the Mo-Tsai scheme.

1. Peaking approximation method

The lack of information about F_1 and F_2 in the early deep inelastic experiments, and the limitation on numerical computing power, had caused difficulties in accurate evaluation of radiative corrections. Mo and Tsai have developed a simplified scheme which involved all the peaking approximations mentioned earlier, in addition to equivalent radiator method to calculate both "internal" and "external" corrections simultaneously [45]. This approach, here after called MTPEAK, was widely used in previous experiments. The corrections calculated in this scheme were estimated to be accurate to few percent, and were not tolerable for our experiment. MTPEAK [45,46] calculations are not described in detail here. We have evaluated the corrections in this scheme only to make a comparison with other results.

2. "Internal" corrections

Bardin *et al.* [42–44] have calculated all the diagrams in Fig. 17 exactly. They have also calculated additional ones to include γ-Z interference, two-photon exchange, and hadronic bremsstrahlung. The exact BARDIN calculations have the most sophisticated and complete treatment for the "internal" radiative corrections and were used in obtaining the results for this experiment. However, it was realized that an alternative program of computing radiative corrections should be explored to check the BARDIN program, since the results presented in this paper depend crucially on radiative corrections. Therefore, we have investigated the Mo-Tsai exact prescription for "internal" bremsstrahlung [64]. This formula was used earlier to calculate quasielastic "internal" contribution for the SLAC experiments [18,17], and by the EMC group for the muon scattering radiative corrections [15]. However, the inelastic contribution in the EMC program did not yield reasonable results in our kinematic range. We, therefore, explored the exact Mo-Tsai scheme carefully, and have realized that some improvements needed to be made before comparing with the BARDIN results. Our exact Mo-Tsai scheme, called MTEXACT, includes some additional terms similar to those in the MTPEAK method to cancel the infrared divergence in the bremsstrahlung diagrams. The BARDIN [42,44] calculations are not described in detail here. Only the terms involved in the computations and improvements made to the Mo-Tsai formalism are discussed. The notation in this section follows Ref. [46] closely, and is not explained here in detail.

a. Bardin et al. calculation

The Bardin *et al.* formulas for internal corrections are given in the Refs. [42–44]. The BARDIN method involved the most complete calculation of radiative cross section, including the gauge invariant taming of the infrared divergent terms. The "internal" correction in the BARDIN program is split into terms

$$\begin{aligned}\delta^B &= \frac{\sigma^i_{\rm rad}(\text{BARDIN})}{\sigma_{\rm Born}} - 1\\ &= \delta^B_h + \delta^B_s + \delta^B_v + \delta^B_t + \delta^B_q + \delta^B_4 + \delta^B_Z . \qquad \text{(B3)}\end{aligned}$$

The "inelastic continuum" contribution from the sum of vertex correction and bremsstrahlung diagrams is given by δ^B_h, in which the infrared divergence is canceled naturally, without the use of any soft photon cutoff. δ^B_s is the soft photon part of the inelastic correction. This term was exponentiated in early versions of the programs using the "variant 1" prescription of Shumeiko [65]. However, for the results presented here exponentiation procedure for soft photon term was *not* used [66]. The vacuum polarization contribution $\delta_{\rm vac}$ is described in detail below as it was also used to improve the MTEXACT scheme. This contribution was "exponentiated" by $\delta^B_v = [2/(1 - \delta_{\rm vac}/2) - 2]$ to include higher-order corrections. The term δ^B_t corresponds to the bremsstrahlung correction from the elastic and quasielastic tails. This term was corrected for the effect of the smeared quasielastic cross section using the calculations from the MTEQUI method discussed below. The hadronic part of the correction δ^B_q calculated within the quark-parton model, the higher-order electromagnetic corrections δ^B_4, and the weak interaction effect δ^B_Z are all typically less than 1% each, in our kinematic range [67]. The theoretical uncertainties at this stage are from the *ad hoc* inclusion or exclusion of higher-order corrections by the various "exponentiation" procedures. Bardin *et al.* have supplied the FORTRAN code to calculate the radiative corrections based on their theoretical work. The code was checked carefully by our group. The BARDIN calculations are based on better theoretical ground, and have become world standard. We, therefore, used them exclusively for our "internal" calculations. However, comparisons with other exact procedures have been used to estimate systematic errors.

b. Exact Mo-Tsai calculation

Complete formulas for the Mo-Tsai calculations are available in Ref. [46]. We have presented in this section some of those formulas that have been improved and included in our calculations. We have not reproduced the long formula for the internal bremsstrahlung, but have referred to the equation number in Ref. [46].

(1) Vacuum polarization. The contribution from the vacuum polarization for electron, muon, and τ lepton loops can be written as [68]

$$\delta^{1}_{\mathrm{vac}} = \frac{2\alpha}{\pi} f(x_l), \tag{B4}$$

where

$$f(x_l) = \frac{-5}{9} - \frac{x_l}{3} + \frac{(2-x_l)^{1/2}(2+x_l)^{1/2}}{6} \times \ln\left[\frac{(1-x_l)^{1/2}+1}{(1-x_l)^{1/2}-1}\right], \tag{B5}$$

$$x_l = \frac{4m_l^2}{-Q^2}, \tag{B6}$$

and m_l is the mass of lepton. Mo and Tsai in their original work used only electron loops for the vacuum polarization diagram. We have added muon, τ and quark loops, which together contribute as much as the electron loop even at SLAC values of Q^2. The quark loops in the vacuum polarization diagram could also be calculated using a similar formula if the quark masses were known, but we have used a parametrization of hadronic vacuum polarization δ^h_{vac} from TASSO Collaboration as used by Bardin *et al.* [69]. The fit to δ^h_{vac}, with corrections for the charges and color factor, summed over all flavors of quarks, and was valid for $1 \leq Q^2 \leq 64$ (GeV/c)^2, and was given by

$$\delta^h_{\mathrm{vac}} = -2\Big(-1.513\times 10^{-3} - 2.822\times 10^{-3}\ln\big(1+1.218Q^2\big)\Big). \tag{B7}$$

With these improvements, the contributions $\delta_{\mathrm{vac}} = \delta^l_{\mathrm{vac}} + \delta^h_{\mathrm{vac}}$ are identical for all programs of Mo and Tsai and Bardin *et al.*

(2) Vertex correction. The nondivergent contribution from the vertex correction diagram is given by [70]

$$\delta_{\mathrm{vert}}(Q^2) = \frac{2\alpha}{\pi}\left[-1 + 0.75\ln(Q^2/m^2)\right]. \tag{B8}$$

(3) Soft photon contribution. The noninfrared divergent part of the soft photon emission cross section yields [70]

$$\delta_{\mathrm{nis}}(Q^2) = \frac{\alpha}{\pi}\left[\frac{\pi^2}{6} - \Phi\left(\cos^2\frac{\theta}{2}\right)\right], \tag{B9}$$

where Φ is the Spence function defined as

$$\Phi(x) = \int_0^x \frac{-\ln|1-y|}{y}dy. \tag{B10}$$

(4) Effective structure function. The above three corrections are included in the factor $F(Q^2)$,

$$F(Q^2) = 1 + \delta_{\mathrm{vac}} + \delta_{\mathrm{vert}} + \delta_{\mathrm{nis}}, \tag{B11}$$

and are multiplied to structure functions F_1 and F_2, or to Born cross section σ_{Born} to form effective structure functions and cross section. These structure functions are then used in the integrals of "internal" bremsstrahlung discussed below.

(5) "Internal" bremsstrahlung. The contribution to radiative cross section from the internal bremsstrahlung can be written as [Eq. (A.24) of Ref. [46] gives the complete formula for the integrand]

$$\sigma_b = \int_{-1}^{1} d\cos\theta_k \int_0^{\omega_m} d\omega\left(A + B\omega + \frac{C}{\omega}\right), \tag{B12}$$

where A, B, and C depend on θ_k, F_1, and F_2, and are weakly varying functions of ω.

The third term in the integrand is infrared divergent. However, this divergence is unphysical and is known to be canceled, to this order, by the divergent part of the vertex correction diagram. Tsai has instead chosen to include, in the expression for σ_b, the multiple soft photon term δ_{soft}:

$$\delta_{\mathrm{soft}}(\omega) = \left(\frac{\omega}{E_0}\right)^{t_r}\left(\frac{\omega}{E'+\omega}\right)^{t_r}, \tag{B13}$$

where

$$t_r = \frac{\alpha}{\pi}\left[\ln\left(\frac{Q^2}{m_e^2}\right) - 1\right]. \tag{B14}$$

The structure functions F_1 and F_2 in the expressions for A, B, and C were replaced by $F(Q^2)F_1$ and $F(Q^2)F_2$ to include the factorized contributions from vacuum polarization and vertex corrections. The inclusion of the δ_{soft} term cancels the infrared divergence, i.e.,

$$\sigma^i_{\mathrm{rad}}(\mathrm{MTEXACT}) = \int_{-1}^{1} d\cos\theta_k \int_0^{\omega_m} d\omega\left(A + B\omega + \frac{C}{\omega}\right) \times\delta_{\mathrm{soft}}(\omega), \tag{B15}$$

is a finite integral. Although, the integral is finite, the integrand rises sharply as ω approaches zero.

To enable accurate numerical computation of the integrals in this method it is necessary to separate soft and hard photons by a cutoff parameter Δ. The analytic formula below the cutoff is given by

$$\int_0^{\Delta} d\omega \frac{C}{\omega}\left(\frac{\omega}{E_0}\right)^{t_r}\left(\frac{\omega}{E'+\omega}\right)^{t_r} \approx \frac{C}{2t_r}\left(\frac{\Delta}{E_0}\right)^{t_r}\left(\frac{\Delta}{E'+\Delta}\right)^{t_r} . \quad \text{(B16)}$$

The value of Δ has to be small enough so that the structure function variation below the cutoff is negligible. Yet, it should be large enough so that the numerical integration above the cutoff is reliable. The best value of Δ for our kinematic region was determined to be 10 MeV, and it was used in our calculations. It should be noted that C depends on angle θ_k and, therefore, it was crucial to perform the angle integration numerically to get reasonable results in this method.

Above the cutoff, the integral was computed using structure function parametrizations for all the physical kinematic region. For the quasielastic and elastic radiative tail contributions, the photon energy integral was first evaluated analytically assuming that the cross section is sharply peaked. The θ_k integral was then evaluated numerically. The continuum radiative cross section thus computed is semiexact as the infrared divergent term was not canceled correctly by the divergent part in the vertex diagram calculation.

3. "External" corrections

Significant improvements to "external" radiative correction have been made by us, over the procedures used in earlier experiments. Our procedure involves a complete calculation of the Mo-Tsai formula for "external" contributions, without any energy peaking approximation.

The measured cross section in the deep inelastic scattering experiment including the straggling of electrons in the target material (with atomic mass A, atomic number Z, and unit radiation lengths x_0 g/cm^2, and thickness T in units of x_0) is given by [71]

$$\sigma_{\text{rad}}^{i+e}(E_0, E', T) = \int_0^T \frac{dt}{T}\int_{E_s^{\text{min}}}^{E_s} dE_s' \int_{E_p}^{E_p^{\text{max}}} dE_p' I(E_s, E_s', t_s(t))\sigma_{\text{rad}}^{i}(E_s', E_p')I(E_p', E_p, t_p(t,T)). \quad \text{(B17)}$$

E_s and E_p are the electron incident and final energies corrected for most probable energy losses Δ_s and Δ_p after passing through a target material before and after scattering point, i.e., $E_s = E_0 - \Delta_s$ and $E_p = E' + \Delta_p$, where

$$\Delta_{s,p} = \frac{\xi_{s,p}}{2}\left[\ln\frac{3\times 10^9 \xi_{s,p} E_{s,p}^2}{2m^2 Z^2} - 0.5772\right] \quad \text{(B18)}$$

and

$$\xi_{s,p} = 1.54\times 10^{-4}\frac{Z t_{s,p} x_0}{A}, \quad \text{(B19)}$$

where $t_{s,p}$ is the radiation length of the material before and after the scattering point, including the shape of the target and the material before and after the scattering point, i.e., $t_s = t_b + t$ and $t_p = t_a + T - t$, where t_b is the material before the target and t_a is the material after the target. The limits of integration (see Fig. 20) are

$$E_p^{\text{max}} = \frac{E_s'}{1 + E_s'(AM)^{-1}(1-\cos\theta)} \quad \text{(B20)}$$

and

$$E_s^{\text{min}} = \frac{E_p}{1 - E_p(AM)^{-1}(1-\cos\theta)} . \quad \text{(B21)}$$

$I(E, E-\omega, t)$ denotes the probability for an electron of energy E to lose an energy ω while traversing material of radiation lengths t due to bremsstrahlung (W_b) and ionization (W_i) losses, and is given by [71]

$$I(E, E-\omega, t) = \frac{1}{\Gamma(1+bt)}\left(\frac{\omega}{E}\right)^{bt}[W_i + W_b(t)] , \quad \text{(B22)}$$

where

$$W_i = \frac{a}{\omega^2}\left(1 + \frac{\omega^2}{E(E-\omega)}\right)^2 , \quad \text{(B23)}$$

$$a = 1.54\times 10^{-4}\frac{Z}{A}, \quad \text{(B24)}$$

$$W_b(t) = bt\frac{\phi(\omega/E)}{\omega}, \quad \text{(B25)}$$

$$\phi(v) \approx 1 - v + 0.75v^2, \quad \text{(B26)}$$

$$b = \frac{4}{3}\left[1 + \frac{1}{12}\left(\frac{Z+1}{Z+\eta}\right)\left(\ln(184.15 Z^{-1/3})\right)^{-1}\right] , \quad \text{(B27)}$$

$$\eta = \frac{\ln(1194 Z^{-2/3})}{\ln(184.15 Z^{-1/3})}, \quad \text{(B28)}$$

and Z is atomic number of material. $\sigma_{\text{rad}}^{i}(E_s', E_p')$ is the "internal" radiative cross section.

The complete calculation of "internal" radiative cross section already involved a double integral, and therefore the full evaluation of radiative cross section σ_{rad} with three additional integrations is impractical. In the evaluation of this integral, an equivalent radiator method had to be used to estimate σ_i at "internal" energies.

The equivalent radiator method, used in computing these "external" corrections, involved using the shape of "external" bremsstrahlung [Eq. (B26)] in including the contribution from "internal" bremsstrahlung (Fig. 17). The magnitude of "internal" bremsstrahlung was included by using two hypothetical radiators each of thickness $t_r = b^{-1}(\alpha/\pi)[\ln(Q^2/m^2)-1]$ radiation lengths, one placed before and one after the scattering point, i.e.,

$$\sigma^{i+e}_{\mathrm{rad}}(E_0,E',T)[\mathrm{MTEQUI}] \approx \int_0^T \frac{dt}{T}\int_{E_s^{\mathrm{min}}}^{E_s} dE_s' \int_{E_p}^{E_p^{\mathrm{max}}} dE_p' I(E_s,E_s',t_s(t)+t_r) \times F(Q'^2)\sigma_{\mathrm{Born}}(E_s',E_p')I(E_p',E_p,t_p(t,T)+t_r). \qquad \text{(B29)}$$

We evaluated the complete radiative cross section $\sigma^{i+e}_{\mathrm{rad}}$, i.e., the triple integral in Eq. (B29), with the above replacements in the regions Q and D of Fig. 20. Analytic integration was performed in the edges of kinematic region, i.e., regions A, B, and C in Fig. 20 to avoid divergences, assuming structure functions do not vary very much.

The "internal" contribution $\sigma^{i}_{\mathrm{rad}}$ in this method [see Eq. (B2)], was evaluated by setting $t_{s,p} = 0$ and dropping the target length integral. For the quasielastic region Q, MTEQUI "internal" calculations were done with and without a smearing correction to the input cross section. The effect of smearing correction was applied to the exact BARDIN calculations to obtain final results. The accuracy of this technique is evaluated below.

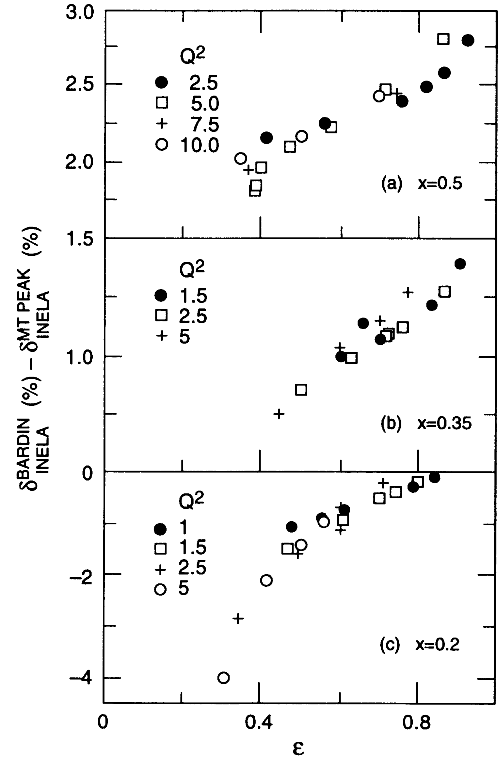

FIG. 21. Comparison of BARDIN versus MTPEAK results for internal correction for the inelastic region of the radiative correction triangle (regions A, B, C, and D of Fig. 20). The MTPEAK program was considered unacceptable due to these large systematic differences in the results within our kinematic range.

4. Comparison of various methods

The "internal" radiative corrections were calculated for all of our kinematic points using the four procedures described above. A comparison of these calculations enabled an estimation of the systematic error on our results.

The differences between MTPEAK and BARDIN internal contributions were large and highly ϵ dependent as shown in Fig. 21. These values of δ_{int} were up to 4% off from the exact calculations. The peaking approximations are indeed expected to fail at small ϵ and x values, where hard photon emission becomes significant, and has motivated our investigations of exact calculations discussed above.

MTEXACT calculations of δ_{inel} and δ_{qel} are compared to BARDIN results in Figs. 22 and 23, respectively. BARDIN

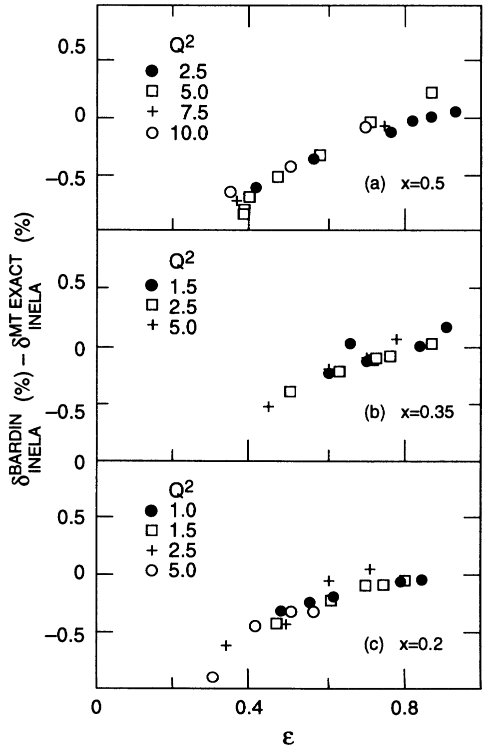

FIG. 22. Comparison of BARDIN versus MTEXACT results for internal correction for the inelastic region of the radiative correction triangle (regions A, B, C, and D of Fig. 20). This favorable comparison at the level of less than 1% provides a bound on our systematic error.

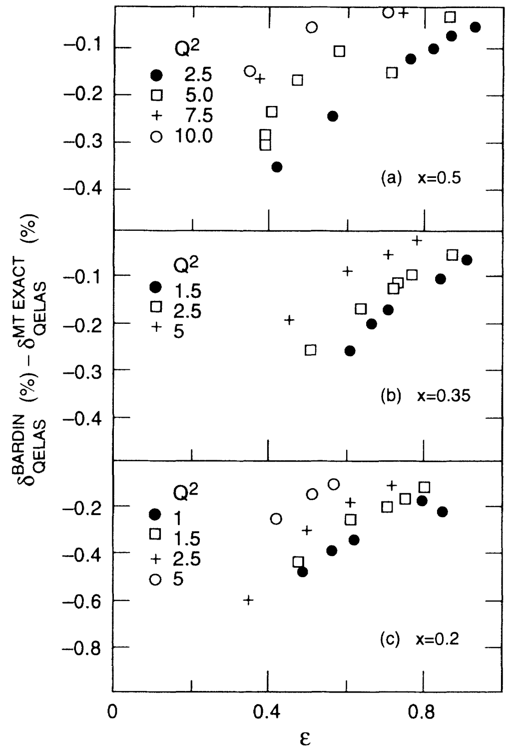

FIG. 23. Comparison of BARDIN versus MTEXACT results for internal correction for the quasielastic region of the radiative correction triangle (region Q of Fig. 20). This favorable comparison at the level of less than 0.5% provides a bound on our systematic error.

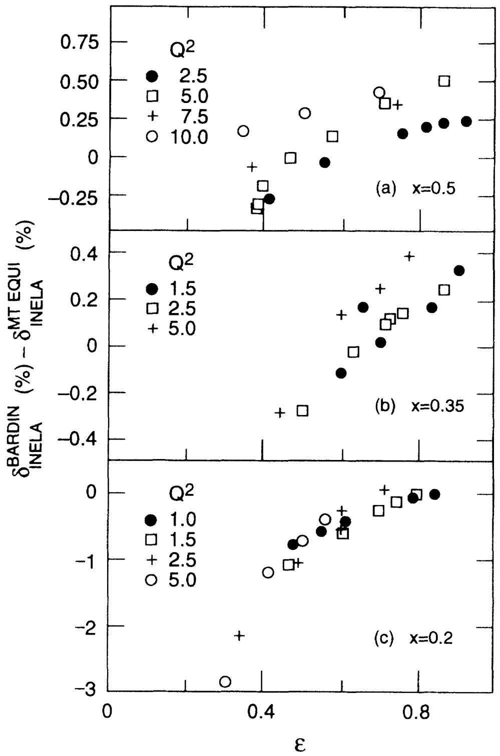

FIG. 24. Comparison of BARDIN versus MTEQUI results for internal correction for the inelastic region of the radiative correction triangle (regions A, B, C, and D of Fig. 20). This level of accuracy of the equivalent radiator program, MTEQUI, is considered adequate for computing the amount of "external" correction.

results, in these comparisons alone, did not include γ-Z interference and hadronic terms, as they were not calculated in the MTEXACT program. The results for δ_{inel} and δ_{qel} agreed to better than about 1% at all of our kinematic points. A systematic error of 1% was assigned to account for possible ϵ-dependent uncertainties in the "internal" corrections. Additional support for the accuracy of these calculations comes from the exclusive muon scattering experiment, where the bremsstrahlung photons were detected [72].

In order to judge the accuracy of the equivalent radiator method [Eq. (B29)] in estimating the "internal" correction we have compared it to BARDIN calculation (see Fig. 24). The differences observed are expected due to the failure of angle peaking approximation. This level of accuracy was sufficient because the internal effects cancel in Eq. (B2).

The level of accuracy of the "external" effects [Eq. (B29)], computed using this approximation, can be directly tested in the experiment by comparing data from targets of different radiation lengths. The radiatively corrected cross section ratio $\sigma_{\mathrm{Fe6}}/\sigma_{\mathrm{Fe2.6}}$ from two Fe targets of radiation lengths 2.6% and 6% used in the experiments averaged over all kinematic points was consistent with unity [$\sigma_{\mathrm{Fe6}}/\sigma_{\mathrm{Fe2.6}} = 1.017 \pm 0.005(\mathrm{stat}) \pm 0.015(\mathrm{syst})$] (see Fig. 25). The systematic error is dominated by the thickness of the thin target. The average difference $R_{\mathrm{Fe6}} - R_{\mathrm{Fe2.6}}$ was $-0.04 \pm 0.04 \pm 0.02$. Since there were not enough data from our experiment, additional tests of the calculations were done using data from an earlier SLAC experiment [58] E139 which measured cross sections from targets of 2%, 6%, and 12% radiation lengths. The 12% data did not agree with the 2% data at small x when MTPEAK radiative corrections were applied [73]. However, when these data were radiatively corrected (for "external" effects) using MTEQUI method, better agreement was found at all x within errors as shown in Fig. 10 of Ref. [58].

We have assigned a systematic error on the ratio $\sigma_{\mathrm{Fe}}/\sigma_{\mathrm{D}}$ of 0.5%, to account for the difference in the radiation lengths of Fe and D targets. The estimate of error on $R_{\mathrm{Fe}} - R_{\mathrm{D}}$ due to "external" corrections is 0.015 assuming that the entire error on the ratio is ϵ dependent.

5. Total radiative correction

The total radiative correction factor applied to the experimental cross sections was given by

$$C_r = \frac{\sigma^{i+e}_{\mathrm{rad}}(\mathrm{MTEQUI})}{\sigma^{i}_{\mathrm{rad}}(\mathrm{MTEQUI})} \frac{\sigma^{i}_{\mathrm{rad}}(\mathrm{BARDIN})}{\sigma_{\mathrm{Born}}}. \qquad \text{(B30)}$$

Table IX lists ranges of individual contributions to the "total" radiative correction δ,

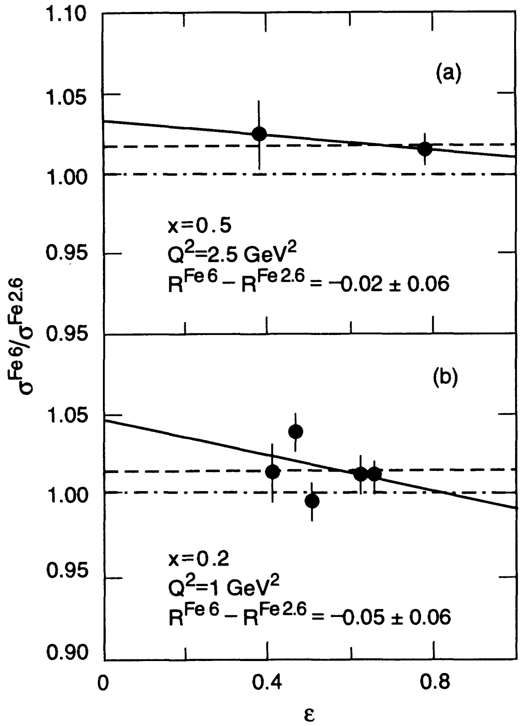

FIG. 25. Ratio of cross sections obtained using two iron targets differing only in thickness, $\sigma^{\text{Fe6}}/\sigma^{\text{Fe2.6}}$, is plotted versus ϵ. The solid line is the best fit and the dashed line is the average value. Except at the lowest ϵ point, the errors are dominated by the target thickness uncertainty of the thin target. Within the accuracy of our data, the ratio is consistent with unity, and, therefore, we see no problems with the "external" radiative correction calculation.

TABLE IX. Minimum and maximum values of different contributions to radiative corrections. Individual contributions may not be combined to get the "total" value as the data are not necessarily for the same kinematic point.

Quantity	Minimum	Maximum
"Internal" corrections (BARDIN)		
δ^i_{inel}	-8.1	20.7
$\delta^i_{\text{qel+el}}$	0.2	8.4
δ^i_{q}	-1.6	-0.1
δ^i_{4}	-0.1	1.2
"Internal" corrections (MTEQUI)		
δ^i_{inel}	-8.3	23.5
$\delta^i_{\text{qel+el}}$	0.1	9.5
"External" corrections (MTEQUI)		
$\delta^{i+e}_{\text{inel}}$	-18.5	32.5
$\delta^{i+e}_{\text{qel+el}}$	0.1	15.3
"Total" correction		
$\delta = 1/C_r - 1$	-17.2	38.3

$$\delta = \frac{1}{C_r} - 1, \tag{B31}$$

in our kinematic range. The error on final cross sections due to these corrections is estimated to be 1% for possible ϵ dependence, and an additional ±1% for any normalization errors. The error on R comes from the ϵ dependence of the error on radiative corrections, and is estimated at ±0.03. The values of radiative correction factors C_r which were multiplied to measured "experimental" cross sections are given in Table V.

[1] E. D. Bloom *et al.*, Phys. Rev. Lett. **23**, 930 (1969).
[2] M. Breidenbach *et al.*, Phys. Rev. Lett. **23**, 935 (1969).
[3] G. Miller *et al.*, Phys. Rev. D **5**, 528 (1972).
[4] A. Bodek *et al.*, Phys. Rev. D **20**, 1471 (1979).
[5] M. D. Mesteyer *et al.*, Phys. Rev. D **27**, 285 (1983).
[6] L. F. Abbott *et al.*, Phys. Lett. **88B**, 157 (1979).
[7] S. Ekelin and S. Fredriksson, Phys. Lett. **162B**, 373 (1985).
[8] G. Altarelli and G. Martinelli, Phys. Lett. **76B**, 89 (1978).
[9] H. Georgi and D. Politzer, Phys. Rev. D **14**, 1829 (1976).
[10] R. Barbieri *et al.*, Nucl. Phys. **B117**, 50 (1976).
[11] A. De Rújula *et al.*, Ann. Phys. (N.Y.) **103**, 315 (1977).
[12] A. Buras *et al.*, Nucl. Phys. **B131**, 308 (1977).
[13] O. Nachtmann, Nucl. Phys. **B63**, 237 (1973).
[14] J. L. Miramontes and J. Sanchez-Guillen, Phys. Rev. D **40**, 2184 (1989).
[15] J. J. Aubert *et al.*, Phys. Lett. **123B**, 275 (1983); G. Bari *et al.*, *ibid.* **163B**, 282 (1985).
[16] A. Bodek *et al.*, Phys. Rev. Lett. **50**, 1431 (1983); **51**, 534 (1983).
[17] R. G. Arnold *et al.*, Phys. Rev. Lett. **52**, 727 (1984); SLAC-PUB-3257, 1983 (unpublished).
[18] S. Stein *et al.*, Phys. Rev. D **12**, 1884 (1975).
[19] E. Berger and F. Coester, Annu. Rev. Nucl. Part. Sci. **37**, 463 (1987).
[20] Bo-Qiang Ma and Ji Sun, Beijing University Report No. Print-86-1217, 1986 (unpublished).
[21] F. E. Close *et al.*, Phys. Lett. **129B**, 346 (1983).
[22] R. D. Smith, Phys. Lett. B **182**, 283 (1986).
[23] E. V. Shuryak, in *Nuclear Physics with Electromagnetic Probes*, Proceedings of the XIth Europhysics Divisional Conference, Paris, France, 1985, edited by A. Gerard and C. Samour [Nucl. Phys. **A446**, 259C (1985)].
[24] S. Dasu *et al.*, Phys. Rev. Lett. **61**, 1061 (1988).
[25] S. Dasu *et al.*, Phys. Rev. Lett. **60**, 2591 (1988).
[26] L. W. Whitlow *et al.*, Phys. Lett. B **250**, 193 (1990).
[27] L. W. Whitlow *et al.*, Phys. Lett. B **282**, 475 (1992).
[28] L. W. Whitlow, Ph.D. thesis, Stanford University, SLAC-Report-357, 1990.
[29] NPAS Users Guide, SLAC-269, UC-28, 1984 (unpublished).

[30] R. B. Neal, *The Stanford Two-Mile Accelerator* (Stanford Linear Accelerator Center, Menlo Park, CA, 1968).

[31] T. Fieguth and S. H. Rokni (private communication).

[32] R. C. Walker, Ph.D. thesis, California Institute of Technology, 1989.

[33] S. Rock *et al.*, Phys. Rev. D **46**, 1 (1992).

[34] J. Mark, *Advances in Cryogenic Engineering* (Plenum, New York, 1984), Vol. 30.

[35] A. Bodek, Nucl. Instrum. Methods **109**, 603 (1973).

[36] R. C. Walker *et al.*, following paper, Phys. Rev. D **49**, 5671 (1994).

[37] S. Dasu, Ph.D. thesis, University of Rochester, 1988.

[38] P. N. Kirk *et al.*, Phys. Rev. D **8**, 63 (1973); L. Mo and C. Peck, SLAC Report No. SLAC-TN-65-29, 1965 (unpublished).

[39] A. Sill *et al.*, Phys. Rev. D **48**, 29 (1993).

[40] A. Bodek, Ph.D. thesis, 1968, MIT Report No. COO-3069-116 (unpublished).

[41] L. S. Rochester *et al.*, Phys. Rev. Lett. **36**, 1284 (1976).

[42] A. A. Akhundov, D. Yu. Bardin, and N. M. Shumeiko, Yad. Fiz. **26**, 1251 (1977) [Sov. J. Nucl. Phys. **26**, 660 (1977)]; JINR Report No. E2-10205 (unpublished).

[43] A. A. Akhundov, D. Yu. Bardin, and W. Lohmann, JINR Report No. E2-86-104 (unpublished).

[44] D. Yu. Bardin and N. M. Shumeiko, JINR Report No. P2-10873 (unpublished).

[45] L. W. Mo and Y. S. Tsai, Rev. Mod. Phys. **41**, 205 (1969).

[46] Y. S. Tsai, SLAC Report No. SLAC-PUB-848 (unpublished).

[47] J. P. Berge *et al.*, Z. Phys. C **49**, 187 (1991); CDHS Collaboration, P. Buchholz, in *Proceedings of International Europhysics Conference on High Energy Physics*, Bari, Italy, 1985, edited by L. Nitti and G. Preparata (Laterza, Bari, 1985).

[48] A. C. Benvenuti *et al.*, Phys. Lett. B **195**, 91 (1987); A. C. Benvenuti *et al.*, *ibid.* **223**, 485 (1989); A. C. Benvenuti *et al.*, *ibid.* **237**, 592 (1990).

[49] J. J. Aubert *et al.*, Nucl. Phys. **B259**, 189 (1985); J. J. Aubert *et al.*, *ibid.* **B272**, 158 (1986).

[50] G. Altarelli and G. Parisi, Nucl. Phys. **B126**, 298 (1977).

[51] H. Abramowicz *et al.*, Z. Phys. C **12**, 289 (1982); B. Vallage, Ph.D. thesis, University of Paris-Sud, 1984.

[52] D. W. Duke and J. F. Owens, Phys. Rev. D **30**, 49 (1984).

[53] J. G. Morfin and W. K. Tung, Z. Phys. C **52**, 13 (1991).

[54] P. N. Harriman *et al.*, Phys. Rev. D **42**, 798 (1990).

[55] A. D. Martin *et al.*, Phys. Rev. D **47**, 867 (1993).

[56] H. Plothow-Besch, CERN program library PDFLIB Users Manual, Version 3.00, 1992.

[57] P. Amaudrus *et al.*, Z. Phys. C **51**, 387 (1991).

[58] J. G. Gomez *et al.*, Phys. Rev. D **49**, 4348 (1994).

[59] D. H. Coward *et al.*, Phys. Rev. Lett. **20**, 292 (1968); A. F. Sill, SLAC Report No. SLAC-NPAS-TN-86-1, 1984 (unpublished).

[60] L. Andivahis *et al.*, SLAC Report No. SLAC-PUB-5753, 1992 (unpublished).

[61] K. L. Brown, SLAC Report No. 75, 1982 (unpublished).

[62] R. Von Gehlen, Phys. Rev. **118**, 1455 (1960); M. Gourdin, Nouvo Cimento **21**, 1094 (1961).

[63] M. Gari and W. Krumpelmann, Z. Phys. A **322**, 689 (1985).

[64] Y. S. Tsai, in *Proceedings of the International Conference on Nuclear Structure* (Stanford University Press, Stanford, CA, 1964), p. 221.

[65] N. M. Shumeiko, Yad. Fiz. **29**, 1571 (1979) [Sov. J. Nucl. Phys. **29**, 807 (1979)].

[66] D. Yu. Bardin (private communication).

[67] D. Yu. Bardin *et al.*, Nucl. Phys. **B175**, 435 (1980); **B197**, 1 (1982).

[68] Y. S. Tsai, *Proceedings of the Asia Pacific Physics Conference* (World Scientific Publishers, Singapore, 1983).

[69] A model for hadronic scattering was taken from TASSO collaboration. TASSO Note 192 (1982). See Ref. [42].

[70] Equation (2.8) of Ref. [46].

[71] Equation (C.1) of Ref. [46]. See also Y. S. Tsai, Rev. Mod. Phys. **46**, 815 (1974), for radiation length definitions.

[72] J. J. Aubert *et al.*, Z. Phys. C **22**, 341 (1984).

[73] J. G. Gomez, Ph.D. thesis, American University, 1987.

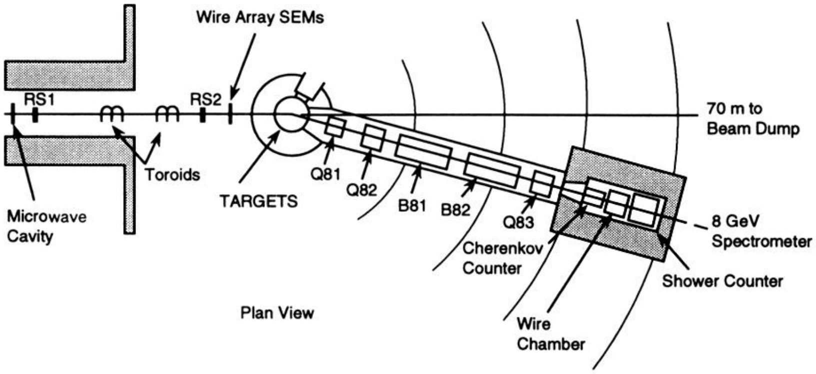

FIG. 1. Floor plan of the experimental hall showing the beam line components, target, and the 8 GeV spectrometer with detectors.

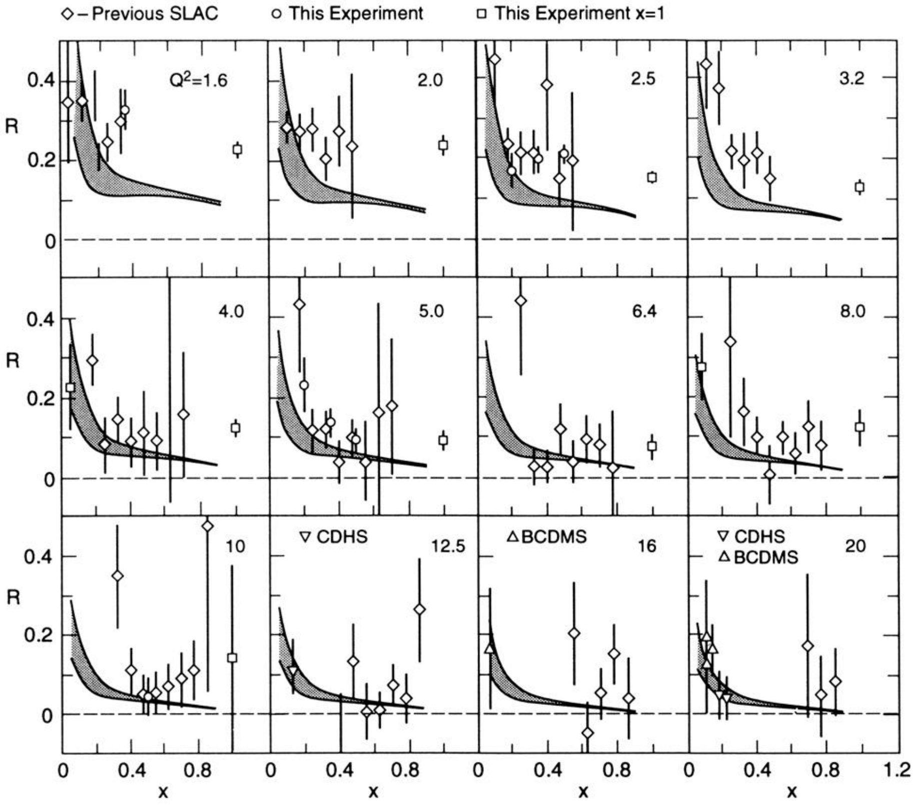

FIG. 12. The values of R, extracted from all previous SLAC data (open diamonds), from inelastic data of this experiment (open circles), and from elastic data of this experiment (open squares), at several values of Q^2, are plotted against x. The errors shown include all statistical and point-to-point systematic errors added in quadrature. The higher Q^2 plots also include data from BCDMS and CDHS. The boldly hashed area is the range of QCD calculations including target-mass effects.

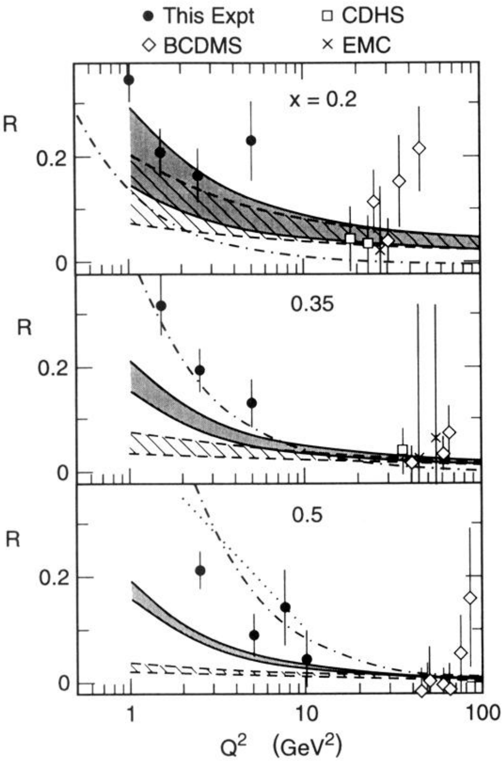

FIG. 8. The values of R at different x (0.2, 0.35, and 0.5), averaged over all targets, are plotted versus Q^2, with all statistical and point-to-point systematic errors added in quadrature. The data from high Q^2 CDHS (ν-Fe), EMC (μ-D), and BCDMS (μ-C/H) experiments are also plotted. The lower lightly hashed band is the range of perturbative QCD predictions for R obtained using various standard quark-gluon distribution functions. The higher boldly hashed band is similarly computed range for QCD including target mass effects. The dot-dashed line is the prediction of the naive parton model. The dotted line for x=0.5 is the prediction of a diquark model.

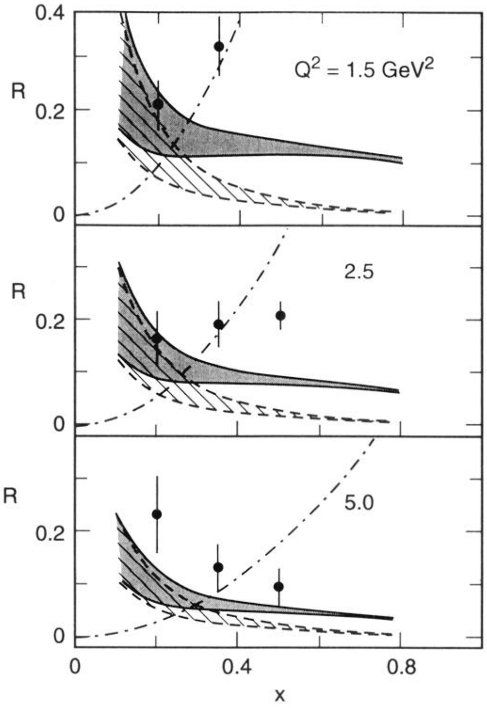

FIG. 9. The values of R at Q^2=1.5, 2.5, and 5 GeV^2 are plotted against x. The errors shown include all statistical and point-to-point systematic errors added in quadrature. The lower lightly hashed band is the range of perturbative QCD predictions for R obtained using various standard quark-gluon distribution functions. The higher boldly hashed band is similarly computed range for QCD including target mass effects. The dot-dashed line is the prediction of the naive parton model.